

intrinsic radiation-resistant nuclear structural materials for high-performance nuclear reactors. An endless composition pool for multiple components, however, causes difficulties in the search for useful HEAs with targeted properties [11]. Therefore, developing fundamental knowledge underlying the extraordinary radiation resistance found in some HEAs is a prerequisite to design HEAs for practical nuclear applications.

Different from traditional nuclear structural alloys with one principal element, HEAs produced by mixing multiple principal elements have several key intrinsic features arising from the random arrangements of constituent elements with diverse chemistry and atomic sizes, all tunable at the atomic level [12–19]: (a) substantial chemical disorder, (b) complex energy landscape with varied energy barriers, and (c) local lattice distortion. These chemical complexity-induced effects fundamentally change the electronic structure, lattice dynamics, and defect dynamics and kinetics in HEAs when compared to pure metals and dilute alloys with translational invariance. The electronic structure and lattice dynamics are closely related to the energy dissipation at the early stage and affect defect evolution at later stages of radiation. This chapter reviews recent theoretical and experimental progress in understanding radiation energy dissipation and the intrinsic chemical effects on defect production and recombination in a collision cascade at the very early stage of radiation damage. The subsequent evolution of defects and microstructure at later stages of radiation damage is reviewed later, and the chemical effects on the microstructure evolution are also discussed. Understanding the effects of intrinsic chemical complexity on radiation-induced defects in HEAs from the early to late stages of radiation will form the basis for designing HEAs as advanced nuclear materials. HEAs in general are considered to contain at least five different elements with the atomic concentration of each element ranging from 5 to 35% [20]. Therefore, HEAs belong to a subset of concentrated solid-solution alloys (CSAs). Unless otherwise noted in this chapter, HEAs specifically represent CSAs with five or more principal elements, and CSAs generally correspond to CSAs with two to four principal elements. Many works have studied the radiation damage in CSAs and HEAs together and demonstrate good radiation tolerance of both. Due to the inherent relationship in terms of chemical complexity and radiation tolerance between CSAs and HEAs, CSAs are discussed along with HEAs. The radiation effects in CSAs provide important information on the correlation of chemical species with radiation performance.

## 12.2 Defect Properties at the Early Stage of Irradiation

Radiation damage occurs when an energetic particle transfers its energy to the irradiated material and target atoms redistribute themselves accordingly [21]. The radiation damage processes include energy transfer to the primary knock-on atom (PKA, approximate time scale,  $10^{-18}$  s), displacement of lattice atoms due to PKA ( $10^{-13}$  s), energy dissipation, defect recombination and clustering ( $10^{-11}$  s), and

defect interaction by thermal migration ( $>10^{-8}$  s). Detailed discussion regarding radiation damage processes has been reviewed by Was [21]. The damage at the early stage generated immediately after particle bombardment through atomic collision and local heating can be defined as primary damage. Radiation damage at the early stage is generally manifested as point defects and small defect clusters. Long-term defect interaction and microstructure evolution ensue from diffusion and migration of these defects. A recent review on primary radiation damage was performed by Nordlund et al. [22]. The radiation damage surviving at the early stage of radiation highly depends on how energy is dissipated and energies for defect formation and migration. Since these defect properties are less dependent on the microstructure of materials, they may be considered as materials' intrinsic resistance to radiation. Wolfer [23] has reviewed the fundamental properties of defects and their role on radiation effects in metals. Below we will review energy dissipation, defect energetics, and defect dynamics at the early stage of radiation in CSAs/HEAs, as compared with conventional metals and dilute alloys.

### 12.2.1 *Chemical Complexity on Energy Dissipation*

When fast-moving particles bombard materials, their energy transfers to both atomic and electronic subsystems, resulting in ballistic displacement and electron excitations. The energy partitioning between these two subsystems depends on the mass and energy of the incident particles. Both computational and experimental studies [24–27] have proved that in general, during ion irradiation with energies lower than 100 keV, radiation damage in alloys is mainly caused by ballistic processes, while at the radiation energy level of GeV, the energy of ions is mostly dissipated through electron excitation without causing obvious lattice damage. Simulations have also showed that the electronic excitation at low energies (~10 keV or lower) needs to be incorporated to elucidate the residual defects and surface particle emission [28, 29]. However, for nuclear applications in the next-generation fission reactors and fusion reactors, materials will be subjected to high neutron fluxes with kinetic energies mainly in the MeV range [1]. In this energy regime, the ballistic displacement process and the electron excitation caused by energetic recoils cannot be considered independently because of comparable energy dissipation to both atomic and electronic subsystems and the energy exchange between these two subsystems induced by electron-phonon (e-ph) coupling [30]. For example, Sellami et al. [31] examined the effect of electronic energy deposition on preexisting radiation damage in single crystal NiCoFeCr CSA irradiated sequentially with 1.5 MeV Ni ions (low-energy irradiation) and 21 MeV Ni ions (high-energy irradiation). Using high-resolution X-ray diffraction, they monitored how the elastic strain developed by low-energy irradiation evolved after high-energy irradiation. Upon electronic energy deposition (21 MeV Ni ion irradiation), the formerly developed elastic strain relaxes due to defect growth caused by the transfer of the electronic energy to the atomic subsystem [31]. Here, note that in nuclear radiation environments, the energy

transfer from the electronic subsystem to the atomic one occurs simultaneously with the defect production, leading to more complex defect production and defect annealing behavior. Nonetheless, the experimental finding of the elastic strain relaxation points out the importance of electronic effects on radiation energy dissipation in CSAs/HEAs.

In the intermediate radiation energy regime (MeV range), the energy dissipation process in metals and alloys is multifold. First, the radiation energy is dissipated in both the atomic subsystem through ballistic collisions and the electronic subsystem through inelastic electronic collisions [32–34]. Second, the energy dissipated to the electronic subsystem can quickly diffuse away as heat because of relatively high electron thermal conductivity in many alloys [34]. Third, the energy dissipated in both subsystems is exchanged further between the electrons and the atoms via e-ph coupling with the electrons acting as a heat source or sink depending on the local temperature difference [32–34]. The extreme chemical disorder in HEAs can produce a significant impact on the processes of energy exchange and heat diffusion by modifying their electronic structure. In addition, the magnetic, electronic, and lattice degrees of freedom are coupled together by the spin-phonon, phonon-magnon, and electron-phonon interactions, further complicating the energy transfer among different subsystems in HEAs [14].

In general, physical properties, such as thermal conductivity, directly control the heat diffusion process in alloys. Thus, studies on the role of the chemical complexity in the thermal conductivity of radiation-tolerant HEAs are of great importance to their uniqueness. Jin et al. [35] measured the thermal diffusivity ( $D$ ) and heat capacity ( $C_p$ ) of pure Ni and some Ni-based CSAs over temperatures ranging from 300 to 1100 K, and further derived their thermal conductivity using  $\kappa = D\rho_T C_p$ , where  $\rho_T$  is the density. They have shown that these Ni-based CSAs (including HEAs) exhibit lower thermal conductivity values than that of pure Ni (Fig. 12.1b). Furthermore, the thermal conductivity values for the Cr-containing CSAs are significantly lower than the other CSAs. In sharp contrast to Ni and CSAs without Cr, the thermal conductivity of these Cr-containing CSAs is similar and increases with increasing temperature from 300 up to at least 1000 K. Such drastic difference between CSAs with and without Cr also exists in their thermal diffusivity, as shown in Fig. 12.1a. These findings reveal that the physical properties of a CSA strongly depend on the type of constituent elements, so understanding the correlation between atomic species and physical properties is critical.

The ab initio Korringa-Kohn-Rostoker coherent potential approximation (KKR-CPA) calculations of the spin-resolved Fermi surfaces of NiCo, NiCoFe, NiCoFeCr, and NiCoFeCrMn CSAs [36] reveal that the minority-spin Fermi surfaces exhibit large disorder smearing for all these CSAs. However, the majority-spin Fermi surfaces of NiCo and NiCoFe CSAs are different from the Cr-containing CSAs (see Fig. 12.2a). By high-resolution Compton scattering experiments, Robarts et al. [37] reveal that in NiCoFeCr CSA, the Fermi surface is significantly smeared across the Brillouin zone (Fig. 12.2b). Like pure Ni, the majority-spin Fermi surfaces of NiCo and NiCoFe CSAs are very sharp, indicating that the majority channel acts as a short circuit for electron conduction. In contrast, the majority-spin Fermi

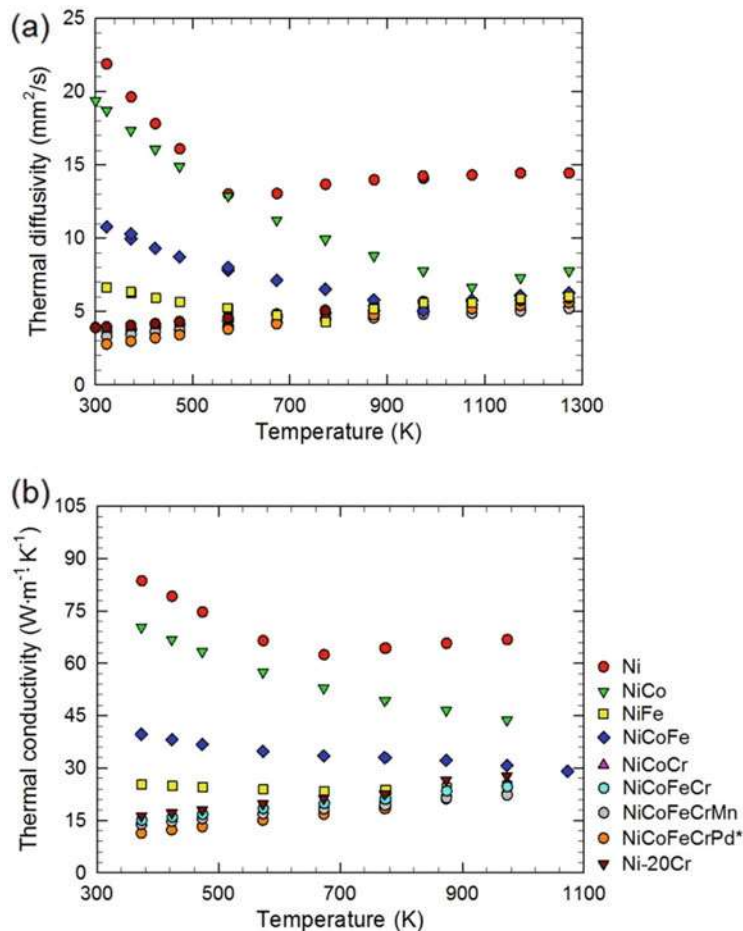


**Fig. 12.1** Temperature-dependent behavior of (a) thermal diffusivity and (b) thermal conductivity of Ni and Ni-containing CSAs. (Adapted from Ref. [35])

surfaces of NiCoFeCr and NiCoFeCrMn are broadened, implying a very short electron mean free path. Consequently, the strong electron scattering leads to low electronic thermal conductivity in the Cr-containing CSAs. Moreover, local lattice distortion and spin disorder also lead to additional electron scattering, but their contribution varies strongly with the composition of HEAs. By performing ab initio calculations on random alloy supercells, Mu et al. [36] found that the displacements of Cr and Mn in NiCoFeCr and NiCoFeCrMn are relatively larger than other elements. Furthermore, while lattice distortion is generally small in face-centered cubic CSAs, adding Pd into NiCoFeCr can clearly increase the atomic displacements, which is consistent with recent experimental observations [38]. They further calculated the contribution of atomic displacement to electron scattering and found its effect is relatively small, ~12% for the NiCoFeCrPd HEA [36]. Additionally, the

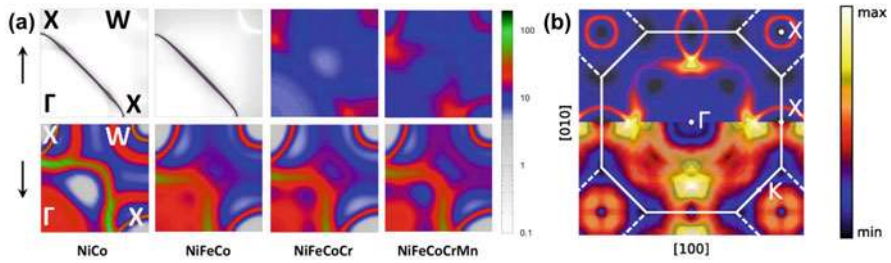


**Fig. 12.2** (a) Calculated Fermi surface in NiCo, NiCoFe, NiCoFeCr, and NiCoFeCrMn CSAs. Majority-spin (top row) and minority-spin (bottom row) channels are separated. (b) Bloch spectral function in the (001) plane of NiCoFeCr CSA, as determined from theoretical calculations (top panel), with the experimental data (bottom panel). (Adapted from Ref. [36, 37])

spin disorder effect on electron scattering has been estimated in NiCoFe, NiCoFeMn, and NiCoFeCrPd. The full spin disorder in these CSAs produces a modest increase of residual resistivity [36].

Zarkadoula et al. [39] investigated effects of the e-ph coupling strength and the electronic thermal conductivity by artificially tuning these two parameters in the molecular dynamics (MD) simulations of a 150 keV PKA cascade in Ni. They found that keeping the same thermal conductivity for a higher e-ph coupling strength, the electronic energy feedback to the atomic subsystem becomes more rapid, leading to reduction of point defects and suppression of the formation of larger clusters [39]. On the other hand, a slightly decreased number of point defects and smaller vacancy clusters occur when lowering electronic thermal conductivity because faster heat dissipation suppresses the point defect recombination in initial damage regions [39].

### 12.2.2 Chemical Complexity on Defect Energetics

The study of defect energetics provides critical information on the relative defect stability of different defect configurations in CSAs/HEAs. Moreover, this atomic-level information also helps one to understand the role of each element in the defect formation. Since local environments vary from one atomic site to another in CSAs/HEAs, the formation and migration energies of point defects in these chemically disordered alloys have a broad distribution rather than a single value, as in the cases of pure metals and dilute alloys.

Ab initio methods, which are based on the density functional theory (DFT), are an established approach to calculate defect energetics, but the presence of the extreme chemical disorder in HEAs is by no means trivial for accurate ab initio calculations. Three techniques have been widely adopted to address the disorder problem in alloys: the coherent potential approximation (CPA) [40], the cluster expansion (CE) [41], and the special quasi-random structures (SQS) [42]. The

CPA is a single-site, mean field approach, while the other two methods mimic the effects of disorder through the construction of supercells with a finite size. The advantage of the CPA method is its high computational efficiency of describing the effect of chemical and magnetic disorder on the configurationally averaged electronic structure. However, its application in the study of defect energetics in HEAs is limited because local structural relaxation is not included [43, 44]. The primary advantage of the supercell methods is that they allow for the internal relaxation of the atomic positions that results from each atom having a different local configuration of surrounding atoms. Additionally, other effects such as short-range order and spin disorder can be included in the supercells naturally [36, 45]. The CE method has been widely employed to study the defect properties in binary CSAs [46, 47]. For binary alloys, a small number of atomic configurations are enough to obtain converged results in the CE method, but the parameterization is computationally expensive for multicomponent alloys even without defects. For the calculations of defect properties in the CE method, vacancies and interstitials are considered as additional species, further increasing the computational cost [47]. The SQS method developed by Zunger et al. [42] constructs a random alloy structure by using a small periodic supercell to mimic the most relevant radial correlation functions of such a random alloy. However, the computational cost is high because the construction of a supercell must be large enough to minimize the spurious interactions for defects.

The SQS method has been widely used to study the defect properties in CSAs. In the SQS supercell, vacancies and interstitials can be modeled by removing or adding specific elements. The formation energy of a point defect,  $E_f(\alpha)$ , represents the energy difference of creating such a defect, calculated by:

$$E_f(\alpha) = E_t(\alpha) - E_t(0) \pm \mu(\alpha) \quad (12.1)$$

Here,  $E_t(\alpha)$  is the total energy of the supercell containing the  $\alpha$  defect,  $E_t(0)$  is the total energy of the perfect supercell, and  $\mu(\alpha)$  is the chemical potential of the  $\alpha$  defect added to or removed from the perfect supercell. The ab initio calculation can directly give the values of  $E_t(\alpha)$  and  $E_t(0)$ . However,  $\mu(\alpha)$  strongly depends on the local environment of the point defect in CSAs. Middleburgh et al. [48] found that unreasonable negative formation energies of vacancies are often obtained in NiCoFeCr CSA when pure metals are used as chemical potential references. To address this problem, Piochaud et al. [49] suggested that the chemical potentials of different elements can be estimated by using the minimum of substitutional energy. By classifying different atoms in binary CSAs according to their nearest neighbors, Zhao et al. [50] developed an efficient calculation method to obtain a good sampling of the substitutional energies while preserving the concentration of the alloys. Although there exist six possible interstitial defect configurations, the [100] interstitial dumbbell has been shown to be the most stable one. Thus, the calculation of interstitial formation energies in CSAs/HEAs is mainly focused on the [100] dumbbell. Figure 12.3 shows the formation energies of [100] dumbbells and vacancies within 256-atom SQS supercells of NiCoCr and NiCoFeCr CSAs obtained from

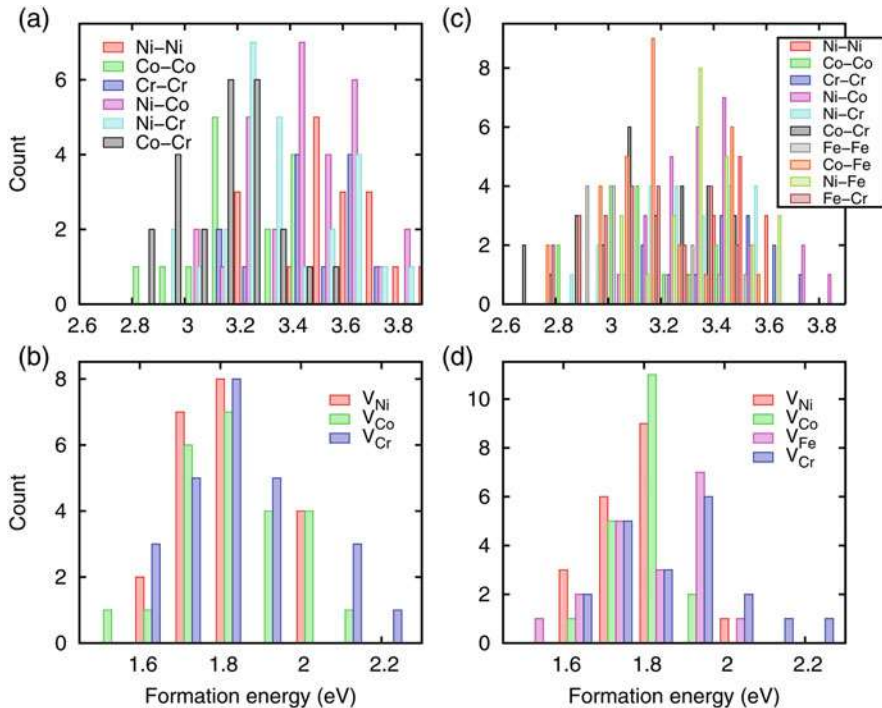


**Fig. 12.3** Formation energies of (a) interstitials and (b) vacancies in NiCoCr CSA and formation energies of (c) interstitials and (d) vacancies in NiCoFeCr CSA. (Adapted from Ref. [51])

DFT calculations [51]. It is found that the Co-Co and Co-Cr dumbbells in the NiCoCr CSA have lower formation energies than the Ni-Ni dumbbells. Similarly, the Co-Co, Co-Fe, and Co-Cr dumbbells in the NiCoFeCr HEA have lower formation energies than the rest of the dumbbells. These results indicate that there is preferable binding of Co interstitials in these CSAs. Consequently, the diffusion of Co interstitials follows chemically biased diffusion channels. For vacancies, the formation energies of the Cr vacancies in both NiCoCr and NiCoFeCr CSAs are higher than other vacancy types. An analysis of the first-nearest-neighbor (1NN) shell surrounding the vacancies [51] reveals that the formation energies decrease with an increasing number of Ni atoms in the 1NN shell of the vacancies. In contrast, increasing the number of Co and Cr atoms in the 1NN shell makes the vacancy formation energies higher. These results demonstrate that vacancies favor Ni-rich or Co- and Cr-poor environments, which can affect the composition distribution around defects.

The migration energies of point defects can be calculated by optimizing saddle-point configurations via the ab initio climbing-image nudged elastic band (NEB) method [50, 52, 53]. In pure Ni without local lattice distortion, the saddle structures of the interstitials and vacancies are located at the midpoint of their diffusion paths [50]. However, the disorder in CSAs/HEAs usually causes a small deviation of the

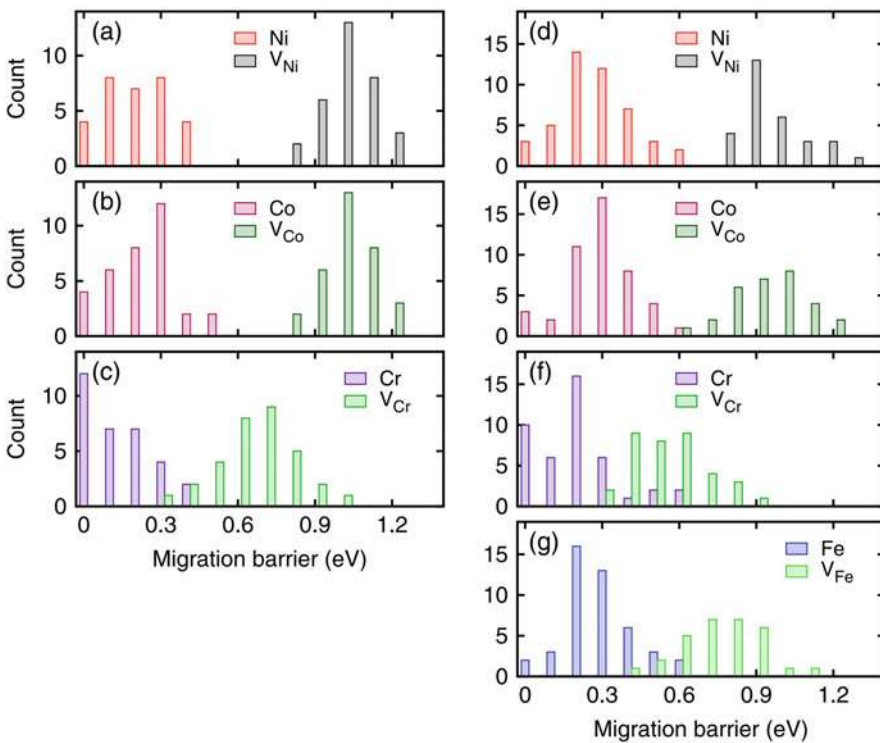


**Fig. 12.4** The migration energies of interstitials and vacancies with respect to each element in (a–c) NiCoCr and (d–g) NiCoFeCr CSAs. (Adapted from Ref. [51])

saddle point from the ideal midpoint. Consequently, the local minimum is determined by optimizing the saddle structure through a quasi-Newton method [54]. Then the migration barrier ( $E_m(\alpha)$ ) can be obtained from the energy difference between the saddle structure ( $E_s(\alpha)$ ) and defective structure ( $E_d(\alpha)$ ), expressed as:

$$E_m(\alpha) = E_s(\alpha) - E_d(\alpha) \quad (12.2)$$

The migration energies of interstitials and vacancies in NiCoCr and NiCoFeCr CSAs are shown in Fig. 12.4. Compared with pure Ni (0.15 eV) [51], the migration energies of interstitials in these two CSAs are higher, indicating slower interstitial diffusion in them. For vacancies, most of their migration energies in the NiCoCr and NiCoFeCr CSAs are lower than the pure Ni case (1.04 eV) [51], suggesting relatively higher diffusion of vacancies in them. In both CSAs, Cr has much lower vacancy migration energies than other types of vacancies, suggesting favorable diffusion vacancy through Cr. From the results, it is apparent that a large overlap region between the interstitial and vacancy migration energies exists for Cr. Because of the strong interaction between the interstitials and vacancies, such an overlap could enhance the recombination of point defects during radiation. The distinct

behavior of the Cr-containing defects closely relates to the flexibility of charge transfer for its partially filled *d* electron orbitals [51]. The ease of charge transfer from the early transition metal Cr to other late transition metals in HEAs can relax the migration barrier. These findings highlight the importance of element type and the effects of electronic structure in the design of radiation-resistant HEAs.

A fundamental process reflecting the intrinsic radiation resistance of materials is the recombination of Frenkel pairs that occurred at the early stage of radiation. The formation and migration energies of defects control defect recombination at the early stage. Zhao et al. [55] recently investigated the recombination process of Frenkel pairs in pure Ni, NiFe, and NiFeCr. They found that adding Fe into Ni increases the spontaneous recombination volume of Frenkel pairs in NiFe CSA, and the recombination probability is remarkably increased by substituting some Fe with Cr in NiFe CSA. The increased recombination probability in CSAs is ascribed to the lower formation energies of Cr- and Fe-containing interstitials and the smaller migration barrier of vacancies in NiFe and NiFeCr CSAs, as compared with pure Ni [55]. This finding clearly shows that the high defect recombination probability is one of the underlying mechanisms for the improvement of radiation resistance in CSAs.

The calculation of migration energies through the NEB method is performed at 0 K with fixed initial and final states in the diffusion path. Therefore, temperature effects are ignored in such calculation, and the diffusion behavior of defects on long time scale cannot be examined through fixed diffusion states. To allow defects to migrate through their optimal diffusion pathway according to the local energy landscape, MD simulations need to be conducted at different temperatures. Both ab initio molecular dynamics (AIMD) and classical MD have been performed to study the diffusion behavior of defects in CSAs. AIMD accurately describes the energy landscape in CSAs at the quantum mechanics level, but the calculation of electronic interactions comes with a high computational cost. Therefore, the size of the supercell and the simulation time in AIMD are limited. Since the diffusion process of defects is a statistical problem, a large amount of defect jumps must be modeled to obtain accurate diffusion coefficients. As a result, classical MD is employed to simulate the diffusion trajectory for a long time. The results of classical MD, however, largely depend on the adopted empirical potentials. Nonetheless, some important insights on the diffusion of point defects can be gained from both AIMD and classical MD. Ossetsky et al. [56] studied interstitial diffusion in a model CSA, NiFe. They found that the diffusion of interstitials is mainly through the Ni channel, and the diffusion of vacancies is mostly through the Fe channel [56]. These preferential mass transport pathways reflect the complex chemical effects on defect energetics in CSAs. The ab initio calculations reveal that the formation energies of Fe vacancies and Ni-Ni and Ni-Fe interstitial dumbbells are lower than other types of defects in NiFe CSA [53]. Thus, these energy-preferred defect structures determine the mass transport pathways.

Besides point defects, the migration behavior of defect clusters also affects the radiation resistance of CSAs. Lu et al. [8] studied the migration trajectories of interstitial clusters in Ni, NiCo, and NiFe at high temperatures through classical MD simulations. Figure 12.5 shows that the interstitial cluster in Ni migrates in a

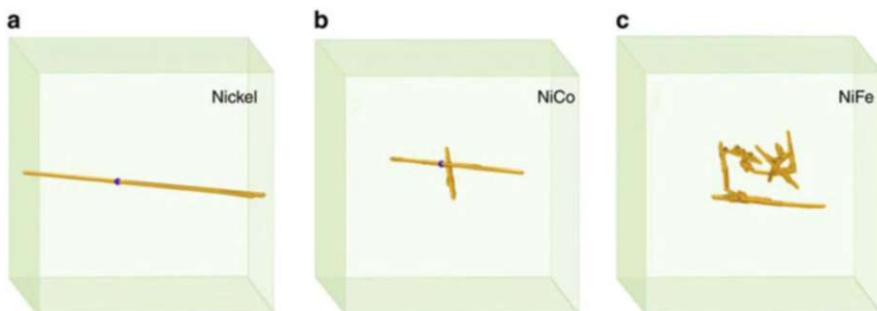


**Fig. 12.5** Migration trajectories of the center of a nine-interstitial cluster in (a) Ni at 800 K, (b) NiCo at 1200 K, and (c) NiFe at 1200 K. (Adapted from Ref. [8])

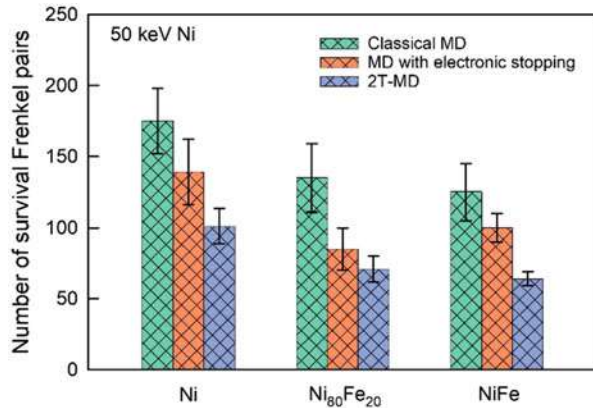
one-dimensional (1D) fashion without changing directions within a 20 ns simulation. However, the migration of the interstitial clusters in NiCo and NiFe CSAs randomly changes direction, and the direction change in NiFe occurs more frequently, leading to a three-dimensional (3D) migration trajectory. The 1D and 3D glide behaviors of interstitial clusters in Ni, NiCo, and NiFe have been confirmed by *in situ* transmission electron microscopy (TEM) characterization [8, 57]. Furthermore, the localized 3D migration behavior for interstitial clusters can increase their recombination probability with less mobile vacancies and vacancy clusters, serving a key role in the suppressed void swelling observed in NiFe, NiCoFe, NiCoFeCr, and NiCoFeCrMn CSAs [8].

### 12.2.3 Chemical Complexity on Defect Dynamics

The fundamental event of defect production is the displacement of an atom from its original lattice site, which requires energy larger than the threshold displacement energy ( $E_d$ ). The  $E_d$  in pure metals and dilute alloys have been investigated extensively via the classical MD simulations [58–61], but their results strongly depend on the interatomic potentials. To address this limitation in the classical MD, AIMD must be utilized to calculate the  $E_d$  particularly in HEAs because of the challenge of developing reliable empirical potentials. Although current AIMD simulations are mainly focused on binary CSAs, important insights can still be gained regarding HEAs. Zhao et al. [62] found that  $E_d$  strongly depends on the local environments by exhibiting a distribution behavior. By inspecting the atomic trajectory of low-energy recoil events in the NiFe, NiCo, Ni<sub>80</sub>Fe<sub>20</sub>, Ni<sub>80</sub>Co<sub>20</sub>, Ni<sub>80</sub>Cr<sub>20</sub>, and Ni<sub>80</sub>Pd<sub>20</sub> CSAs [62], they found that the threshold energies are mainly determined by a chemical disorder effect and less affected by the local lattice distortion.

To study the collision cascade formed in the intermediate radiation energy regime for long time and large length scales, MD simulation is utilized. As mentioned earlier, the electronic effects on defect production and evolution cannot be ignored.

**Fig. 12.6** A comparison of average surviving damage in the classical MD cascade, the MD cascade including electronic stopping force, and the 2T-MD cascade at the end of the simulation for 50 keV Ni cascades in Ni, Ni<sub>80</sub>Fe<sub>20</sub>, and NiFe. (Data is from Refs. [32, 39, 64])



Electronic energy loss has been occasionally included in cascade simulations, but the challenge has been to consider the effect of the e-ph coupling on defect dynamics. The two-temperature molecular dynamics (2T-MD) model, as developed by Duffy and Rutherford [29, 63], has been recently applied to investigate the e-ph coupling effect on collision cascades in CSAs, and the equation of motion is modified as:

$$m_i \frac{\partial V_i}{\partial t} = F_i(t) - (\gamma_s + \gamma_p)V_i + \tilde{F}(t) \quad (12.3)$$

$V_i$  is the velocity of atom  $i$  with mass  $m$ , subject to a force  $F_i(t)$  due to its interactions with surrounding atoms. Two friction terms,  $\gamma_s$  and  $\gamma_p$ , are introduced to account for the energy loss due to the electron stopping and the e-ph interaction, and  $\tilde{F}(t)$  is a random stochastic force term to include the energy gain from the electronic to the atomic subsystem.  $\tilde{F}(t)$  is determined by the local temperature of the electronic subsystem, and the evolution of the electronic temperature is described via the heat diffusion equation (see details in [29, 63–65]). The other challenge for the MD simulations is the development of empirical interatomic potentials for HEAs. As a result, the e-ph coupling effect recently integrated in MD simulations of collision cascades has been mainly focused on binary and ternary CSAs with reliable interatomic potentials.

Several general features about the collision cascade after the inclusion of the e-ph coupling effect have been identified by a comparison study of classical MD, MD including the electron stopping, and 2T-MD for pure Ni and some CSAs [32, 33, 39, 64]. Figure 12.6 shows the number of surviving Frenkel pairs at the end of the simulation time (45 ps) for 50 keV Ni cascades averaged over 12 events in Ni, Ni<sub>80</sub>Fe<sub>20</sub>, and NiFe. In the 2T-MD model, the inclusion of the two friction terms leads to a significant reduction of the number of surviving defects, revealing the key role of the electronic effects on the defect production. Zarkadoula et al. [64] studied the evolution of the number of displaced atoms with time for 50 keV cascades in Ni<sub>80</sub>Fe<sub>20</sub>, Ni<sub>80</sub>Cr<sub>20</sub>, and Ni<sub>40</sub>Fe<sub>40</sub>Cr<sub>20</sub> CSAs through the classical MD, the MD with

the electronic stopping, and the 2T-MD simulations. It was found that the inclusion of electronic stopping in the classical MD reduces the peak number of displaced atoms, and the peak number further decreases after consideration of both electronic stopping and the e-ph coupling effect in the 2T-MD simulation [64]. It is expected that the addition of electronic energy dissipation from the PKA, i.e., the electronic stopping, can slow down fast-moving atoms, leading to less damage produced in the cascade. The e-ph coupling further reduces the number of displaced atoms as determined in the 2T-MD simulation, which is related to the defect recombination process. While the electronic temperature can be much higher than the atomic temperature in the  $fs$  time frame under MeV and GeV ion bombardments, the situation is different at much lower energies, e.g., induced by 30 or 50 keV ions. At the start of the collision cascade from keV ions, the atomic temperature rises rapidly, several orders higher than the electronic temperature, due to the ballistic collision [33, 64]. This thermal spike assists defect recombination, which results in less surviving defects after the dynamic annealing process [65]. An analysis of the temporal evolution of the maximum atomic temperature in the 2T-MD cascade [33, 64, 65] reveals that the activation of the e-ph coupling slows down the quenching rate of the atomic temperature, indicating an energy feedback from the electronic subsystem to the atomic one. Through the 2T-MD simulations, Zarkadoula et al. [39] further demonstrate that the stronger the e-ph coupling strength, the faster the energy transfer from the electronic subsystem to the atomic one. This energy feedback channel further assists the recombination of defects produced during the current cascade event. Attention also should be paid to the competition process of transferring energy away from the thermal spike. Since the atomic temperature can be much higher than the electronic temperature in some local regions, electrons can act as heat sinks to cool down the excited atomic subsystem due to the e-ph coupling [65]. Meanwhile, because of the high electronic thermal conductivity in metals and alloys, the heat transferred from the atoms to electrons can diffuse away from the cascade, providing a cooling channel for the thermal spike. However, the 2T-MD simulations show that the effect of the cooling channel is less than that of the energy feedback channel. Consequently, there is less net production of defects than those in the classical MD and the MD including the electronic stopping only (see Fig. 12.6).

Moreover, the results in Fig. 12.6 also reveal that adding Fe and increasing the concentration of Fe can suppress defect production, which is qualitatively consistent with the trend found in the relative backscattering yield measurements [7]. It is worth mentioning that MD simulation is not a reliable way to study the effect of different chemical species on defect production because the interatomic potential is another major factor that determines defect structures. As mentioned above, the early transition metal, Cr, can tune the electronic structure of Ni-containing CSAs dramatically, benefiting their radiation performance. Based on Rutherford backscattering results, Gihan et al. [66] recently reported that  $Ni_{40}Fe_{40}Cr_{20}$  CSA is more radiation tolerant than  $Ni_{80}Fe_{20}$  CSA under 1.5 MeV Mn ion irradiation at room temperature (RT). The 2T-MD simulations, however, predict that the  $Ni_{80}Fe_{20}$  CSA would exhibit better radiation tolerance [64].

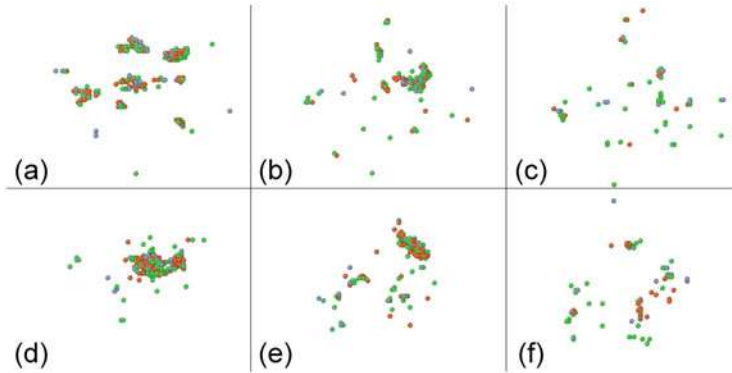


**Fig. 12.7** Surviving interstitials (top panel) and vacancies (bottom panel) in (a, d) the classical MD, (b, e) the MD with electronic stopping force, and (c, f) the 2T-MD at the end of a 50 keV Ni cascade simulation (80 ps) in Ni<sub>40</sub>Fe<sub>40</sub>Cr<sub>20</sub> CSA. Green, orange, and purple highlight the Ni, Fe, and Cr interstitials or vacancies, respectively. (Adapted from Ref. [64])

Additionally, the inclusion of both the e-ph coupling and the electronic stopping in the 2T-MD model imposes a significant impact on how defects are arranged into clusters [32–34, 39, 64]. Figure 12.7 shows that the surviving interstitials and vacancies of a representative 50 keV 2 T-MD cascade in Ni<sub>40</sub>Fe<sub>40</sub>Cr<sub>20</sub> CSA exist in the form of more isolated point defects and smaller defect clusters when compared to the defect morphology in the classical MD and the MD with the electronic stopping. Many studies [26, 65, 67] have shown that the defect clustering is originally driven by the thermal spike. However, the additional energy dissipation through the electronic stopping reduces the net energy to produce a thermal spike. Furthermore, the e-ph coupling allows heat transfer from the thermal spike to the electronic subsystem since the atomic temperature in the thermal spike is significantly higher than the electronic temperature. Zarkadoula et al. [32, 64] examined the alloying effect on the clustering behavior through 2T-MD simulations. They found that alloying Fe, Cr, or Pd with Ni dramatically increases the fraction of isolated defects and reduces the average cluster size. The addition of Pd into Ni results in a very high fraction of isolated interstitials [32] because interstitial clusters are less stable in the NiPd CSA with strongly distorted local lattices [68].

While the majority of the MD studies focused on binary and ternary CSAs due to the limitation of potentials for CSAs with more than three elements, a recent work by Lin et al. [69] studied defect generation and evolution in NiCoFeCr CSA during primary damage. Compared with pure Ni, fewer defects survived at the end of the displacement cascade with PKA energies from 10 to 50 keV, as shown in Fig. 12.8. They found that although the production of displaced atoms during the thermal spike phase in NiCoFeCr CSA was larger, more interstitials and vacancies were recombined due to an enhanced thermal spike and low thermal conductivity, leading to fewer surviving defects. Moreover, the relatively smaller binding energies

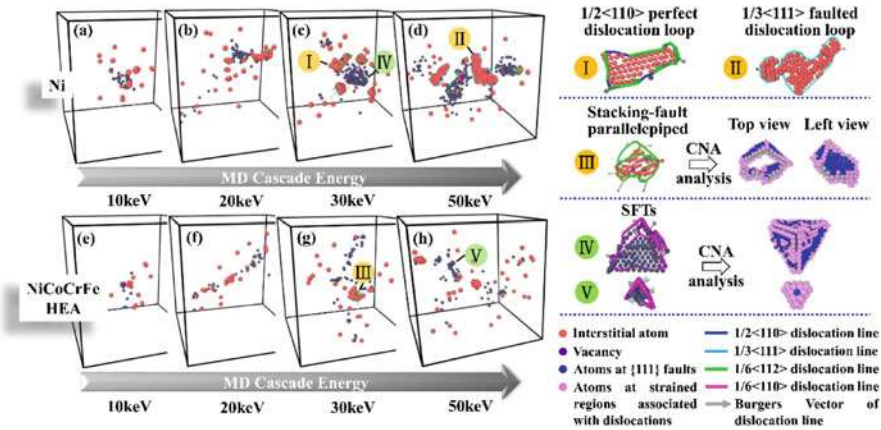


**Fig. 12.8** Survived defects in pure Ni (top panel, a–d) and in NiCoFeCr CSA (bottom panel, e–h) at the end of displacement cascades with the PKA energy from 10 to 50 keV. Details of dislocation loops and stacking faults are shown in the right panel. (Adapted from Ref. [69])

between interstitials delayed interstitial clustering in NiCoFeCr CSA. As a result, the damage accumulation is suppressed more in NiCoFeCr CSA than pure Ni.

On the other hand, oversized atoms act as strong trapping sites for vacancies, which suppress the clustering process of vacancy-type defects. Yang et al. observed that the average size of defect clusters decreases as the atomic size mismatch factor increases in Ni and Ni-based binary CSAs [70, 71]. Tong et al. [38] quantitatively measured the evolution of local lattice distortion in Ni-based CSAs under ion irradiation at RT. They observed a relaxation of local lattice distortion at low radiation doses (0.1, 0.3, and 1 displacement per atom, dpa) for NiCoFeCr and NiCoFeCrMn as a result of the larger lattice expansion induced by interstitial-type defects [38]. Oppositely, they showed that the local lattice distortion in NiCoFeCrPd HEA is enhanced under irradiation since the local lattice distortion in its pristine condition is large enough to overcome the effect of the overall lattice expansion [38]. It is worth pointing out that the extent of the local lattice distortion strongly depends on the composition and crystal structure. A very large local lattice distortion has been reported for the loosely packed body-center cubic CSAs containing Zr and/or Hf [18], but their radiation performance has not been evaluated. In addition, the local lattice distortion in CSAs varies from one atomic site to another due to the changing charge transfer effect in different local atomic environments [72]. Zhao et al. [51] have demonstrated that charge transfer can reduce the migration energy barrier of defects, which promotes defect recombination as discussed earlier. Note that charge transfer among different elements has a preference in terms of electronegativity. The preference for charge transfer is not only responsible for chemical biased mass transport but also related to the formation of short-range chemical order in CSAs. Zhao et al. [73] recently simulated the diffusion of point defects in ordered and disordered NiFe CSAs. They demonstrated that chemical ordering slows down the diffusion of point defects due to the decrease of effective coordination numbers

for defect jumps [73]. All these studies mentioned here provide important insight on radiation damage control by tuning local lattice distortion and charge transfer effect. These two effects can surely be tailored to control defect migration behavior through careful selection of alloying elements and composition.

## 12.3 Defect and Microstructure Evolution upon Radiation

Upon irradiation, the microstructure of materials evolves along with the production of defects. The microstructural evolution generally gives rise to tailored physical and mechanical properties of irradiated materials. Moreover, the radiation resistance of materials can be evaluated by measuring the microstructural evolution through detailed characterization of defects generated during irradiation. Development of advanced techniques, such as electron microscopy, X-ray spectroscopy, atom probe tomography, and Rutherford backscattering spectrometry, allows for the state-of-the-art characterization of defects ranging from point defects, to defect clusters, to dislocations, to precipitates, to secondary phases, and to cavities. Evolution of defects in response to irradiation is tied by specific irradiation conditions, including dose, dose rate, temperature, particle species, etc. The influence of irradiation conditions on microstructure has been systematically reviewed by Was [21] and Zinkle [74]. Previous reviews have summarized microstructure changes under irradiation in pure metals [75–79], steels [80–83], and nanostructured materials [3, 4, 84]. In this section, we focus on the microstructural evolution in CSAs/HEAs upon radiation damage. The mechanical behavior of HEAs after irradiation is beyond the scope of this chapter, and some discussion on this topic can be found in [85–88]. Atomic-level homogeneity and physical characteristics of CSAs have been reviewed by Zhang et al. [89, 90]. Here, by comparing with conventional alloys, we reveal distinct microstructural changes in CSAs/HEAs, and discuss how these changes are related to their fundamentally different defect behaviors and properties. Potential strategies to enhance the radiation resistance of CSAs/HEAs will be discussed.

### 12.3.1 Damage Accumulation and Defect Evolution Under Low Radiation Doses

The microstructure of materials evolves with radiation damage. Under very low radiation doses, microstructural changes are generally associated with the formation of point defects and very fine clusters, and under high radiation doses, extended defects, element segregation, or secondary phases can emerge. The point defects and small clusters are very sensitive to Rutherford backscattering spectrometry (RBS) and X-ray spectroscopy. RBS/channeling (RBS/c) experiments revealed that even at

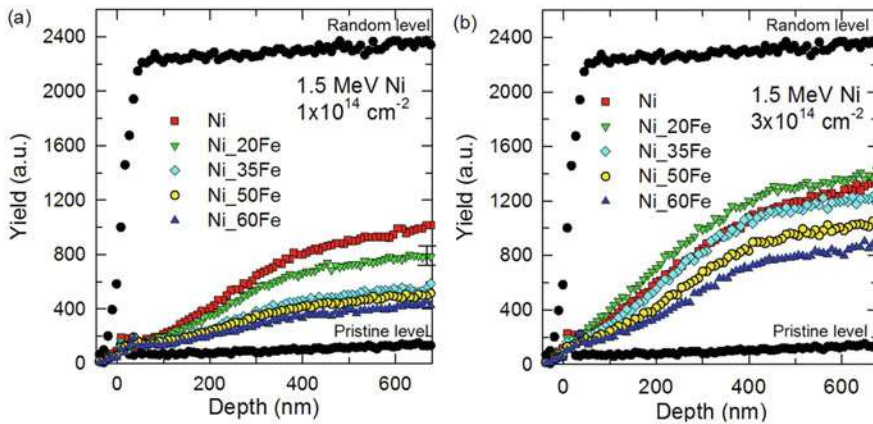


**Fig. 12.9** Accumulated damage in a series of  $\text{Ni}_{1-x}\text{Fe}_x$  CSAs irradiated with 1.5 MeV Ni ions at RT. The fluence is (a)  $1 \times 10^{14} \text{ cm}^{-2}$  and (b)  $3 \times 10^{14} \text{ cm}^{-2}$ , corresponding to  $\sim 0.13$  and  $0.4$  dpa, respectively. (Adapted from Ref. [91])

a dose as low as several percent of a dpa, the chemical concentration and composition variation observably affect the accumulated radiation damage in CSAs. In  $\text{Ni}_{1-x}\text{Fe}_x$  CSAs irradiated by with 1.5 MeV Ni ions at RT, even though the concentration dependence on radiation-induced hardening is not obvious, RBS/c experiments show that an increase of Fe concentration from 0 to 60 atomic percent (at. %) leads to less accumulated damage, as shown in Fig. 12.9 [91]. Moreover, accumulated radiation damage can be readily seen in the irradiated  $\text{Ni}_{1-x}\text{Fe}_x$  CSAs for as low as  $\sim 0.13$  dpa, and with the increase of dose from  $\sim 0.13$  to  $0.4$  dpa, more damage accumulates in these alloys. TEM characterization results also confirmed that the defect size decreases and the defect density increases with increasing Fe concentration from Ni, to  $\text{Ni}_{80}\text{Fe}_{20}$ , to NiFe. The less accumulated radiation damage, as a function of Fe concentration, could be a result of encouraged defect recombination and is consistent with the MD simulations in  $\text{Ni}_{1-x}\text{Fe}_x$  CSAs (Fig. 12.6) [32, 39, 64]. In the Ni-based CSAs irradiated with 3 MeV Au ions at RT, it is also evident that less radiation damage is accumulated in NiFe than NiCo or Ni for ion doses as low as  $\sim 0.06$  dpa [92]. The underlying reason for the lower irradiation damage is partly due to the enhanced defect recombination in NiFe CSA that is associated with the 3D migration of interstitial clusters (Fig. 12.5) [8].

Moreover, beyond certain radiation doses, accumulated damage can saturate and migrate to depths deeper than the SRIM-predicted (SRIM stands for stopping and range of ions in matter code) damage profile due to the mechanical stress generated by irradiation-induced defects. The saturation dose has been shown to be lower in less radiation-resistant alloys. For instance, under 3 MeV Au ion irradiation at RT, the saturation dose for Ni, NiCo, and NiFe is  $\sim 0.3$ ,  $0.6$ , and  $1.8$  dpa, respectively [92]. By combining the results gained from RBS/c and TEM characterization, Lu et al. [93] have demonstrated that the defect range and size decrease from Ni, to NiCo, to NiFe, which is attributed to the defect recombination rate and diffusion of

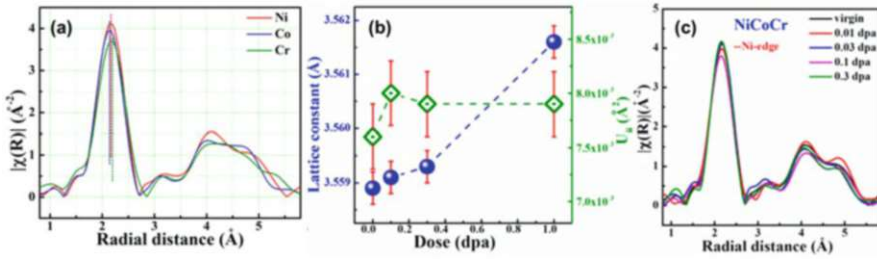


**Fig. 12.10** Evolution of bonding and lattice constant in irradiated NiCoCr CSA. (a) K-edge of Ni, Co, and Cr measured by EXAFS. The slight difference between the first peak positions indicates different bond length of Ni, Co, and Cr with its surrounding atoms. (b) Lattice constant and Debye-Waller factor as a function of dose. (c) EXAFS spectrum as a function of dose. (Adapted from Ref. [97])

defects. Besides the effect of alloying elements, Fan et al. [94] have shown that temperature also plays an important role in defect range through in situ RBS/c experiments performed at various temperatures. In NiFe CSA irradiated with 1.5 MeV Ni ions at temperatures ranging from  $-123$  to  $227$   $^{\circ}\text{C}$ , defect saturation and migration beyond the predicted damage range are more significant at lower temperatures. This trend may be due to the higher density of smaller defects formed at lower temperature that can generate a higher mechanical stress and larger lattice strain, thereby promoting the defect migration into deeper depths. Moreover, post-irradiation annealing heals the radiation damage via the coalescence and growth of smaller defects, which in turn reduces the accumulated lattice strain and mechanical stress, leading to damage retraction to shallower depths. In order to avoid the effects of temperature on defect accumulation, in situ RBS/c at cryogenic temperature was performed. Under 500 keV Ar irradiation at 16 K, compared with Ni and NiFe CSA, less damage is observed in NiCoFeCr CSA from as low as  $\sim 0.152$  to 6 dpa [95]. The in situ RBS/c experiments performed at very low doses and low temperatures demonstrate the inherent resistance to irradiation damage in certain CSAs/HEAs, which agrees with the fundamental properties of CSAs/HEAs as discussed in the previous section.

Local atomic environments in pristine CSAs/HEAs can vary site by site due to chemical complexity and can be modified even under very low radiation dose. In Ni-ion irradiated  $\text{Ni}_{80}\text{Pd}_{20}$  and  $\text{Ni}_{50}\text{Pd}_{50}$  CSAs (multiple energies from 2 to 16 MeV were applied to achieve approximately uniform damage from surface up to 3500 nm), extended X-ray absorption fine structure (EXAFS) analysis has revealed that the fraction of Pd-Pd pairs decreases with irradiation from  $\sim 0.01$  to  $0.1$  dpa and then increases at 0.3 dpa [96]. In pristine NiCoCr CSA, the pair distribution function (PDF) does not exhibit observable lattice distortion. However, the EXAFS revealed short-range-order with favorable bonding between Cr and Ni/Co that can be enhanced with irradiation damage, as can be seen in Fig. 12.10 [97]. The potential short-range-order has been shown to affect the mechanical properties of HEAs [98, 99], and its role in radiation resistance deserves future investigation. It is evident

that lattice constants and bonding evolve with dose in irradiated NiCoCr CSA even as low as 0.01 dpa (Fig. 12.10b, c). In general, due to the large size mismatch, more severe lattice distortion is measured in Pd-containing alloys, such as NiPd and NiCoFeCrPd, than alloys belonging to the subsystems of NiCoFeCrMn HEA with similar atomic size [38, 97, 100]. Yang et al. [38] have showed that as compared with NiCoFeCr and NiCoFeCrMn, a larger lattice distortion in NiCoFeCrPd HEA delayed the growth of dislocation loops after irradiation.

Furthermore, X-ray measurements revealed elastic strain in NiFe and NiCoFeCr CSAs irradiated with 1.5 MeV Ni irradiation at RT, but not in pure Ni [31]. The strain could arise from the formation of smaller defect clusters and increases with irradiation dose from  $\sim$ 0.04 dpa, and high electronic energy deposition by 21 MeV Ni irradiation can trigger defect recombination that can relax the developed strain. These studies show that lattice distortion or strain can exist in pristine CSAs/HEAs due to the atomic size mismatch, and evolves with the formation and evolution of defects due to irradiation. Furthermore, the microstructure changes at very low damage levels generally involve fine defect clusters, lattice strain, and bonding, which may not be readily characterized by electron microscopy. However, these microstructure changes can have direct or indirect impact on element segregation, dislocation growth, or the formation and growth of cavities under prolonged irradiation damage, since these local microstructure changes could affect the nucleation and migration of defects.

### 12.3.2 *Radiation-Induced Segregation and Precipitation*

Radiation-induced point defects and defect clusters can be immobile, or mobile to recombine with other defects, or migrate to defect sinks. Defect fluxes generally favor certain constituent elements over others, and the coupled fluxes of defects and elements lead to radiation-induced segregation (RIS) around defect sinks. For a binary CSA, such as  $A_xB_y$ , the segregation trend around defect sinks can be estimated by the ratio of diffusion coefficients [21]:

$$\frac{d_i^A}{d_i^B} - \frac{d_v^A}{d_v^B} \quad (12.4)$$

where  $d_i^A$  and  $d_i^B$  are the interstitial diffusion coefficients for elements A and B, respectively, and  $d_v^A$  and  $d_v^B$  are the vacancy diffusion coefficients for elements A and B, respectively. Since interstitial migration transports elements along its migration direction and vacancy migration exchanges with elements into the opposite direction, larger diffusivity ratio of interstitials over vacancies can result in enrichment of the elements around defect sinks, and vice versa. Therefore, a positive  $\frac{d_i^A}{d_i^B} - \frac{d_v^A}{d_v^B}$  indicates that element A will be enriched around defects. Through  $\mu$ s-scale MD simulations, Osetsky et al. [101] calculated the diffusion coefficients in  $Ni_{1-x}Fe_x$

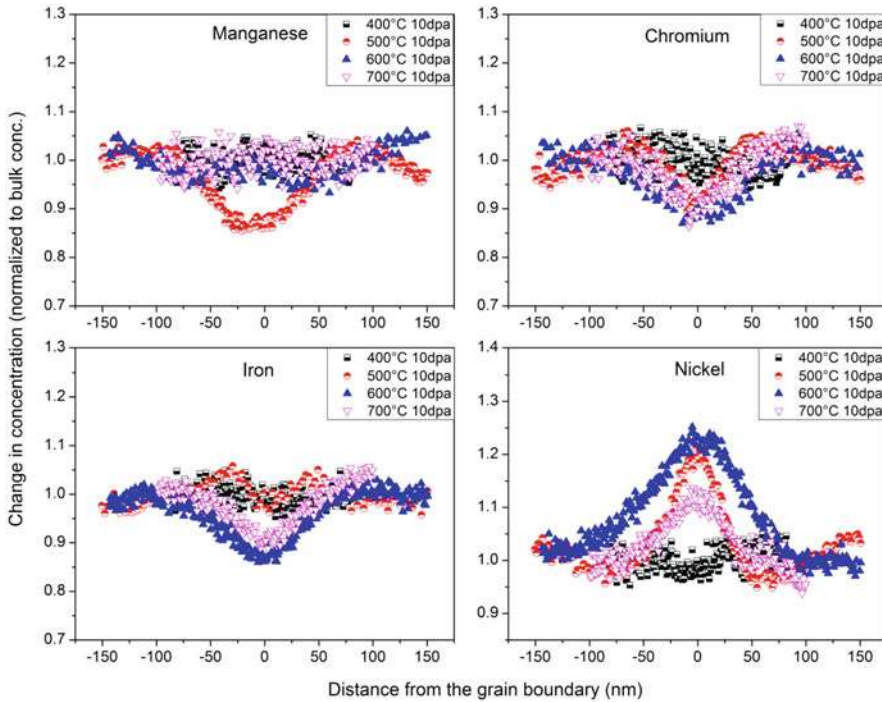


**Fig. 12.11** RIS at the grain boundary of each element with respect to irradiation temperature from 400 to 700 °C in Ni-irradiated  $\text{Fe}_{0.27}\text{Ni}_{0.28}\text{Mn}_{0.27}\text{Cr}_{0.18}$  CSA to 10 dpa. (Adapted from Ref. [87])

CSAs and showed that interstitial diffusion through Ni is preferred, while vacancy diffusion through Fe is preferred. In other words, Eq. 12.4 yields a positive (negative) value for Ni (Fe), suggesting Ni enrichment (Fe depletion) around defects in  $\text{Ni}_{1-x}\text{Fe}_x$  CSAs. Through STEM-EELS (electron energy loss spectroscopy) measurements, Wang et al. [102] confirmed the Ni enrichment and Fe depletion around helium bubbles in  $\text{Ni}_{1-x}\text{Fe}_x$  CSAs irradiated with 200 keV helium ions at 500 °C, and showed that the amount of segregation decreases from NiFe, to  $\text{Ni}_{65}\text{Fe}_{35}$ , and to  $\text{Ni}_{80}\text{Fe}_{20}$ . While the segregation trend of binary CSAs may be straightforward to predict and understand, the RIS in HEAs becomes complicated due to multiple constituent elements.

RIS at grain boundaries in Ni-irradiated  $\text{Fe}_{0.27}\text{Ni}_{0.28}\text{Mn}_{0.27}\text{Cr}_{0.18}$  CSA to 10 dpa is found to be less significant from 400 to 700 °C compared with FeCrNi-based austenitic steels under similar irradiation conditions [87]. Moreover, the amount of Ni enrichment and Fe/Cr depletion reaches the maximum at 600 °C, but the maximum depletion of Mn occurs at 500 °C (Fig. 12.11). This result suggests that the temperature dependence of RIS for different elements varies in CSAs/HEAs. In general, the maximum amount of solute segregation occurs at intermediate temperatures, and the amount of solute segregation in alloys is highly dependent on the defect recombination rate and the mobility of defects [21]. A higher defect

recombination rate decreases the flux of defects to sinks and thus reduces segregation, and a lower mobility of defects also decreases the flux of defects to sinks and thus reduces segregation. At lower temperatures, the limited mobility of vacancies leaves a high concentration of irradiation-induced vacancies and thus enhances the vacancy-interstitial recombination rate, which in turn reduces segregation. At high temperatures, the high concentration of thermal vacancies not only increases the diffusion of alloying elements to sinks but also leads to a high vacancy-interstitial recombination rate. The former factor increases segregation, but the latter factor decreases segregation. At intermediate temperatures, both interstitials and vacancies are mobile, and due to a lower concentration of thermal vacancies and irradiation-induced vacancies, the defect recombination rate is low. Therefore, a significant amount of defects flow to defect sinks, resulting in substantial segregation at intermediate temperatures. For FeCrNi-based austenitic steels, the peak segregation temperature ranges from 300 to 500 °C, which is affected by composition, dose rate, and other irradiation conditions [21, 103]. However, as discussed earlier, the peak segregation temperature for the  $\text{Fe}_{0.27}\text{Ni}_{0.28}\text{Mn}_{0.27}\text{Cr}_{0.18}$  CSA ranges from 500 to 600 °C, higher than FeCrNi-based austenitic steels, which could be a result of multiple principal constituent elements. The composition and concentration of constituent elements in CSAs/HEAs tailor the defect mobility and defect recombination. They also modify the formation energies of vacancies and the thermal stability of vacancy clusters, which in turn modifies the thermal vacancy concentration at different temperatures. All these factors affect the temperature at which each element in an HEA is segregated most. The temperature-dependent segregation for each element in an HEA and the complicated segregation mechanism call for careful selection of the working temperatures for HEAs.

In  $(\text{NiCoFeCr})_{97.6}\text{Al}_{2.4}$  HEA irradiated with Au ions to 31 dpa at temperatures ranging from 250 to 600 °C, Ni/Co is enriched and Fe/Cr/Al is depleted around dislocation loops [104]. The enrichments of Ni/Co and depletion of Fe/Cr around dislocations and voids are also observed in other NiCoFeCr-based HEAs under different irradiation conditions [105–109]. Figure 12.12a shows that Ni/Co is enriched and Fe/Cr is depleted around voids in Ni-irradiated NiCoFeCr CSA at 500 °C. Moreover, this segregation trend is similar to segregation in irradiated FeCrNi-based austenitic steels, where Ni enriches and Fe/Cr depletes [103, 110, 111]. The RIS in NiCoFeCr-based HEAs can be understood from the different migration energies of interstitials and vacancies through the constituent elements. The interstitial migration energy through different elements in NiCoFeCr CSA is similar, with the highest for Co (~0.348 eV) and the lowest for Cr (~0.211 eV) [109]. However, the vacancy migration energy through all elements can vary significantly. Vacancy migration favors Fe and Cr (~0.799 and 0.587 eV) over Ni and Co (~1.021 and 0.982 eV). The element-dependent migration energy variation leads to a larger (smaller) diffusivity ratio of interstitials over vacancies for Ni/Co (Fe/Cr). In other words, the result of Eq. 12.4 is positive for Ni/Co and negative for Fe/Cr in NiCoFeCr CSA. Therefore, Ni/Co (Fe/Cr) enriches (depletes) around defects. The segregation trend indicates that vacancy migration could dominate RIS in NiCoFeCr-based HEAs.

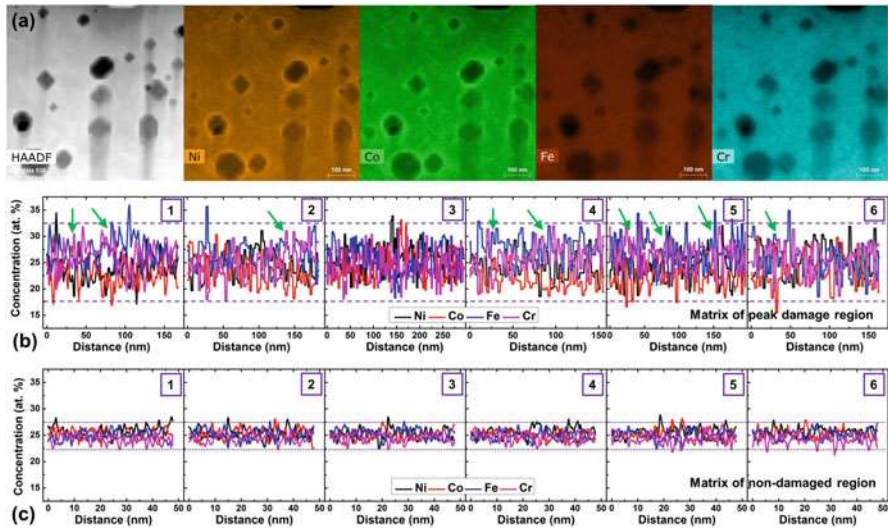


**Fig. 12.12** Element segregation in NiCoFeCr CSA irradiated with 3 MeV  $\text{Ni}^{2+}$  ions to 106 dpa at 500 °C. (a) HAADF-STEM image and the corresponding STEM-EDS maps around the peak damage region. Ni/Co is enriched and Fe/Cr is depleted around voids. EDS line scan profiles in the matrix of (b) the peak damage region and (c) outside of the ion-damaged region. (Adapted from Ref. [109])

Besides RIS around defects, the matrix concentration also evolves due to irradiation damage. In Ni-ion irradiated NiCoFeCr CSA [109], the matrix concentration profiles have large fluctuations in the peak damage region (Fig. 12.12b), while the matrix in the non-damaged region seems to be highly disordered without clear elemental segregation (Fig. 12.12c). It has been shown that in NiCoFeCr irradiated by 3 MeV Ni ions at 500 °C to 86 dpa (196 dpa under full cascade mode) and 580 °C to 54 dpa (123 dpa under full cascade mode), the matrix chemical concentration varies as a function of irradiation damage and depth [112]. In the matrix, Fe/Cr is enriched in depth shallower than ~900–1000 nm, and Ni/Co is enriched in depth deeper than ~900–1000 nm until the end of ion-damaged region. Moreover, up to 54 dpa, very few voids form in depth shallower than ~900–1000 nm despite the high dislocation density in the region, while in depth deeper than ~900–1000 nm, high-density voids form. This finding demonstrates that the matrix chemical concentration variation is closely associated with defect migration and void evolution. However, a clear correlation between the matrix concentration change and defect evolution in CSAs/HEAs is not fully understood.

While the high-entropy effect facilitates the formation of single-phase solid solution in a variety of pristine HEAs, irradiation can lead to the formation of secondary phases or precipitates along with RIS. In Ni-irradiated (NiCoFeCr) $\text{Al}_{0.12}$  HEA at 500 °C to high doses (~106 dpa),  $\text{Ni}_3\text{Al}$  type nanoprecipitates in the form of  $\text{L1}_2$  ordered structure formed in the matrix [113]. However,  $\text{Ni}_3\text{Al}$  was not found in non-irradiated (NiCoFeCr) $\text{Al}_{0.12}$  that underwent the same thermal history, which

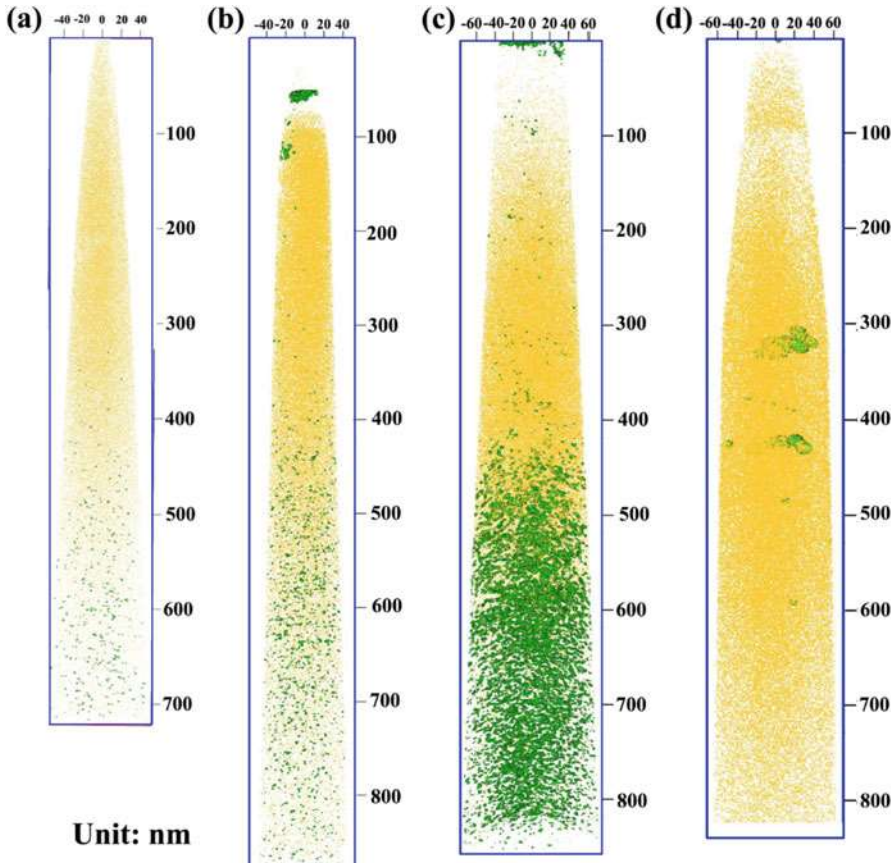


**Fig. 12.13** Constructed Ni iso-concentration surfaces (green surface) from atom probe tomography of  $(\text{NiCoFeCr})\text{Al}_{0.3}$  HEA irradiated with 3 MeV Au ions at (a) 250 °C, (b) 350 °C, (c) 500 °C, and (d) 650 °C. The deposited Au ions are indicated by yellow color. (Adapted from Ref. [108])

suggests that radiation-enhanced diffusion may facilitate the formation of precipitates. For NiCoFeCr HEA without Al, no precipitates were observed under the same irradiation condition. This finding shows that the doping element in HEAs can directly affect RIS and structural changes during irradiation. Furthermore, in  $(\text{NiCoFeCr})\text{Al}_{0.3}$  HEA irradiated with 3 MeV Au ions, formation and evolution of precipitates are found to be dependent on both temperature and irradiation depth [108]. As shown in Fig. 12.13, nanoprecipitates ( $\text{L1}_2$  ordered structure) were formed in the non-irradiated region (depth beyond 500 nm) from 250 to 500 °C, and the size of precipitates increased with increasing temperature. While at 650 °C, no precipitates were found in the non-irradiated region, and relatively larger nanoprecipitates ( $\text{B}2$  ordered structure) were present inside the ion-damaged region (shallow than 500 nm). The depth and temperature-dependent precipitation behavior are explained by the competition between ballistic dissolution and radiation-

enhanced diffusion. At lower temperatures (250 to 500 °C), irradiation suppressed the formation of precipitates in the ion-irradiated region because of irradiation-induced ballistic mixing, while at higher temperatures (650 °C), precipitation in the ion-irradiated region was enhanced due to radiation-enhanced diffusion.

It has been shown that under thermal treatment, disordered arrangements of elements in the matrix of pristine  $(\text{NiCoFeCrCu})\text{Al}_{1.3}$  HEA could remain, despite element segregation, decomposition, and precipitation due to multiple principal elements [114]. The introduction of precipitates or secondary phases could lead to improved radiation resistance, since the interface between them and the matrix can serve as defect sinks. W-based refractory HEAs with second-phase particles have been reported to suppress the formation of irradiation-induced dislocation loops under 1 MeV Kr irradiation up to 8 dpa at 800 °C [85]. This finding indicates that local element segregation can coexist with the high-entropy effect and may not undermine the radiation resistance of HEAs. Furthermore, the preexisting stable precipitates may serve as defect sinks to relieve radiation damage in HEAs. Cao et al. [115] revealed that in  $(\text{CoCrFeNi})_{94}\text{Ti}_2\text{Al}_4$  HEAs irradiated with 4 MeV Au ions at RT from 10 to 49 dpa, the HEA with nanoprecipitates exhibited smaller dislocation loops and less hardness change, as compared with the HEA without nanoprecipitates. The underlying reasons for the delayed defect growth are attributed to the disordering and dissolution of nanoprecipitates. As discussed earlier,  $\text{Ni}_3\text{Al}$  type nanoprecipitates was observed in Ni-irradiated  $(\text{NiCoFeCr})\text{Al}_{0.12}$  HEA at 500 °C but not found in the non-irradiated  $(\text{NiCoFeCr})\text{Al}_{0.12}$  HEA which had undergone the same thermal treatment [113]. It is evident that the precipitates or secondary phases, regardless of whether preexisting or formed due to thermal treatment or irradiation, may only be stable under certain temperatures or radiation doses. The size and distribution of precipitates or secondary phases and the stability of them against thermal treatment and irradiation would affect their sink strength. The stable structures of pristine HEAs due to the high-entropy effect may experience significant structural and chemical changes under radiation, which calls for the careful selection of elements in HEAs for nuclear energy applications. How irradiation-induced segregation and precipitation will evolve under prolonged radiation still deserves detailed investigations.

### ***12.3.3 Evolution of Cavities and Dislocations at Elevated Temperatures***

Irradiation-induced large cavities are detrimental to the structural stability of nuclear materials. As potential structural materials for advanced nuclear systems, cavities in CSAs/HEAs have been intensively studied. Detrimental cavities generally are considered to include voids and bubbles, both of which are three-dimensional vacancy clusters. Internal pressure and gas species can be absent in voids, where bubbles are

pressurized and contain gas species, such as helium. The nucleation of voids is associated with vacancy supersaturation ( $S_v$ ) and can be expressed as below [21]:

$$S_v = C_v / C_v^o \quad (12.5)$$

where  $C_v$  is the vacancy concentration in the bulk solid and  $C_v^o$  is the thermal equilibrium vacancy concentration. Therefore, a larger  $S_v$  indicates that there is a larger driving force for void nucleation. Also, a lower vacancy formation energy would lead to a larger  $C_v^o$ , thus decreasing  $S_v$  and the corresponding driving force for void nucleation. Furthermore, a higher vacancy-interstitial recombination rate would lead to fewer surviving vacancies after irradiation and thus a smaller  $C_v$ , which in turn decreases  $S_v$  and void nucleation. The nucleation of bubbles depends not only on  $S_v$  but also on the gas atoms inside and the internal pressure. The growth rate for a cavity,  $(\frac{dR}{dt})$ , which includes both voids and bubbles, can be estimated by [21]:

$$\frac{dR}{dt} = \frac{\Omega}{R} (D_v(C_v - C_v^s) - D_i(C_i - C_i^s)) \quad (12.6)$$

where  $R$  is the cavity radius,  $\Omega$  is the atomic volume,  $D_v$  and  $D_i$  are, respectively, the vacancy and interstitial diffusivity,  $C_v$  and  $C_i$  are, respectively, the vacancy and interstitial concentration in the bulk solid, and  $C_v^s$  and  $C_i^s$  are the vacancy and interstitial concentration around the cavity surface, respectively. It is important to note that the internal gas pressure plays a role in  $C_v^s$  and  $C_i^s$  for bubbles. Equation 12.6 shows that smaller difference in the influx between vacancies and interstitials would lead to a smaller cavity growth rate.

The variation in the concentration and composition has been shown to directly affect cavity growth in helium-irradiated CSAs/HEAs. Helium bubble size decreases with increasing Fe concentration in  $Ni_{1-x}Fe_x$  CSAs (0 to 50 at. %) irradiated with 200 keV helium ions at 500 °C to  $5 \times 10^{16} \text{ cm}^{-2}$ , and small dislocation loops were present in  $Ni_{1-x}Fe_x$  CSAs in contrast to extended dislocation networks in pure Ni [102]. Through STEM-EELS, they also found a higher helium density in helium bubbles in  $Ni_{1-x}Fe_x$  with higher Fe concentration, which may lead to higher gas pressure and stabilization of smaller helium bubbles. A combination of a higher defect recombination rate, denser nucleation sites, and higher helium density contributes to the suppression of helium bubble growth in  $Ni_{1-x}Fe_x$  with a higher Fe concentration.

Moreover, helium bubbles in binary  $Ni_{80}X_{20}$  CSAs (X = Co, Fe, Cr, Mn, Pd) irradiated with 200 keV helium ions at 500 °C to  $1 \times 10^{16} \text{ cm}^{-2}$  show a clear composition dependence, and the overall cavity size is the largest in  $Ni_{80}Co_{20}$  and smallest in  $Ni_{80}Mn_{20}$  [116]. As discussed previously, defect recombination in certain CSAs is much higher than dilute alloys or single element metals. An increased vacancy-interstitial recombination will lead to a lower concentration of vacancies and interstitials ( $C_v$  and  $C_i$ ) that results in a reduced cavity growth rate, as can be determined from Eq. 12.6. The smaller helium bubble size in  $Ni_{80}Mn_{20}$  can also be a result of closer diffusivity values for the vacancies and interstitials due to the smaller

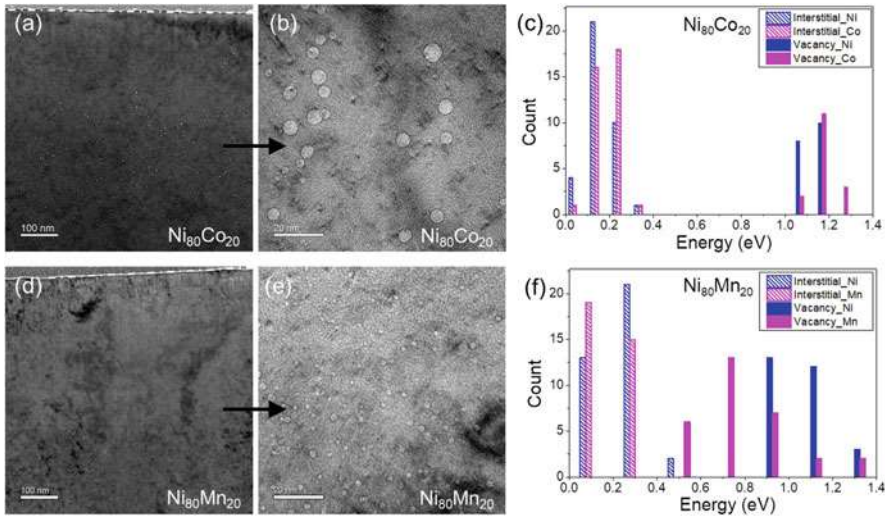


**Fig. 12.14** Helium bubble distribution and defect energetics in  $\text{Ni}_{80}\text{Co}_{20}$  and  $\text{Ni}_{80}\text{Mn}_{20}$  CSAs. Under-focused TEM images show the overall helium bubble distribution in (a)  $\text{Ni}_{80}\text{Co}_{20}$  and (d)  $\text{Ni}_{80}\text{Mn}_{20}$ , and bubble size comparison in (b)  $\text{Ni}_{80}\text{Co}_{20}$  and (e)  $\text{Ni}_{80}\text{Mn}_{20}$  under 200 keV  $\text{He}^+$  ion irradiation at 500 °C. The free surface is denoted as the dash-dot line. Vacancy and interstitial migration energies in (c)  $\text{Ni}_{80}\text{Co}_{20}$  and (f)  $\text{Ni}_{80}\text{Mn}_{20}$  are calculated from DFT. (Adapted from Ref. [116])

gap between the migration energies of vacancies and interstitials in  $\text{Ni}_{80}\text{Mn}_{20}$ , as shown in Fig. 12.14. A large variation in diffusivities between vacancies and interstitials could lead to separation of vacancies and interstitials, so  $C_v$  and  $S_v$  (vacancy concentration and vacancy supersaturation) can be high in some local regions, leading to growth of larger helium bubbles. Similar diffusivities could lead to a smaller influx difference of vacancies and interstitials toward existing helium bubbles, and thus a smaller cavity size, as in the case of  $\text{Ni}_{80}\text{Mn}_{20}$ . Besides defect migration energy, defect formation energy is also found to affect helium bubble distribution. Compared with other binary  $\text{Ni}_{80}\text{X}_{20}$  CSAs,  $\text{Ni}_{80}\text{Pd}_{20}$  has a much smaller vacancy formation energy, which leads to a larger  $C_v^0$  (thermal equilibrium vacancy concentration) [116] and thus a smaller  $S_v$  (vacancy supersaturation), as shown in Eq. 12.5. As a result, growth of helium bubble is suppressed. A larger  $C_v^0$  could also contribute to a higher diffusion rate of vacancies and helium atoms, which results in a broader distribution of helium bubbles in  $\text{Ni}_{80}\text{Pd}_{20}$ , which is confirmed by experiments [116]. It should be noted that for these  $\text{Ni}_{80}\text{X}_{20}$  CSAs, an irradiation temperature of 500 °C was applied which corresponds to 0.45 to 0.52  $T_M$  (melting temperature) and is close to their peak swelling temperature [116].

Chen et al. [117, 118] showed that when irradiated below and above the peak swelling temperature (250 to 700 °C), the helium bubble size in  $\text{NiCoFeCr}$  CSA is consistently smaller than in pure Ni. They also attributed the underlying reason to the closer migration energies for vacancies and interstitials in  $\text{NiCoFeCr}$  CSA. Besides

comparing the helium bubble size in CSAs/HEAs with pure Ni, Yang et al. [119] also showed that the bubble size in NiCoFeCrMn HEA was relatively smaller than in 304 stainless steels after helium irradiation at 500 °C. In addition to helium bubble evolution in CSAs/HEAs, there are also limited studies on helium diffusion in CSA/HEAs. A first-principles study shows that as compared to pure Ni, both interstitial and substitutional diffusions of helium atoms require a higher energy in NiCoFeCr CSA, indicating that there is less helium mobility in NiCoFeCr CSA [120]. In NiCoFeCr HEA, helium diffusion through a dissociation mechanism is favored at low vacancy concentrations, whereas a vacancy mechanism is favored at supersaturated vacancy concentrations. Both experimental and simulation studies demonstrated that chemically tailored defect energetics in certain CSAs/HEAs can promote defect recombination, tune defect diffusivity, reduce helium mobility, and modify helium distribution.

Although the chemical complexity in CSAs/HEAs can suppress the size of helium bubbles, the distribution of these bubbles reflects the irradiation damage profile from SRIM calculation under both high- and low-energy helium irradiations (Fig. 12.14a, d), which is analogous to pure metals or dilute alloys [116, 118]. In contrast, the void distribution in CSAs/HEAs can be different from conventional alloys. For pure metals and dilute alloys, void formation and growth at different irradiation depths generally corresponds to the ion-induced radiation damage at each depth, and the amount of void swelling generally reflects the ion-induced radiation damage profile. However, for certain CSAs/HEAs irradiated to relatively high doses, voids are absent around the region containing the peak radiation damage, and only small voids form near and beyond the ion-irradiated range (outside of the dislocation range). Figure 12.15 shows that in pure Ni or NiCo irradiated with both 1.5 and 3 MeV Ni ions at 500 °C, the majority of swelling resides around the peak radiation damage region. However, in CSAs/HEAs, such as NiFe, NiCoFe, NiCoFeCr, and NiCoFeCrMn CSAs, no voids form in the peak damage region, and negligible void swelling occurs outside of the ion-irradiated range [121].

This unusual void distribution does not necessarily occur in all CSAs. The void distribution in NiCo CSA is more similar to pure Ni rather than NiFe-based or NiCoFeCr-based CSAs. This is attributed to the similar defect energetics between Ni and NiCo. Defect migration and formation energies in NiCo have a very narrow distribution and are very close to pure Ni [122]. In contrast, in NiFe and NiCoFeCr CSAs, defect energetics have a very broad distribution, and the average defect energetics vary significantly from pure Ni [95]. Moreover, current studies show that the unusual void distribution in certain CSAs/HEAs can arise from two factors. On the one hand, interstitial clusters in some CSAs/HEAs are found to migrate via a 3D mechanism, which is different from the 1D migration in pure metals [121, 123]. Limited mobility of interstitial clusters avoids the rapid growth of dislocations, and encourages vacancy-interstitial recombination, thus reducing the vacancy concentration. On the other hand, point defect migration (both vacancies and interstitials) shows strong preference over certain elements. For instance, due to the preferential diffusion, Fe/Cr is depleted and Ni/Co is enriched around voids in NiCoFeCr-based HEAs. The size and depth of the voids do affect the amount of

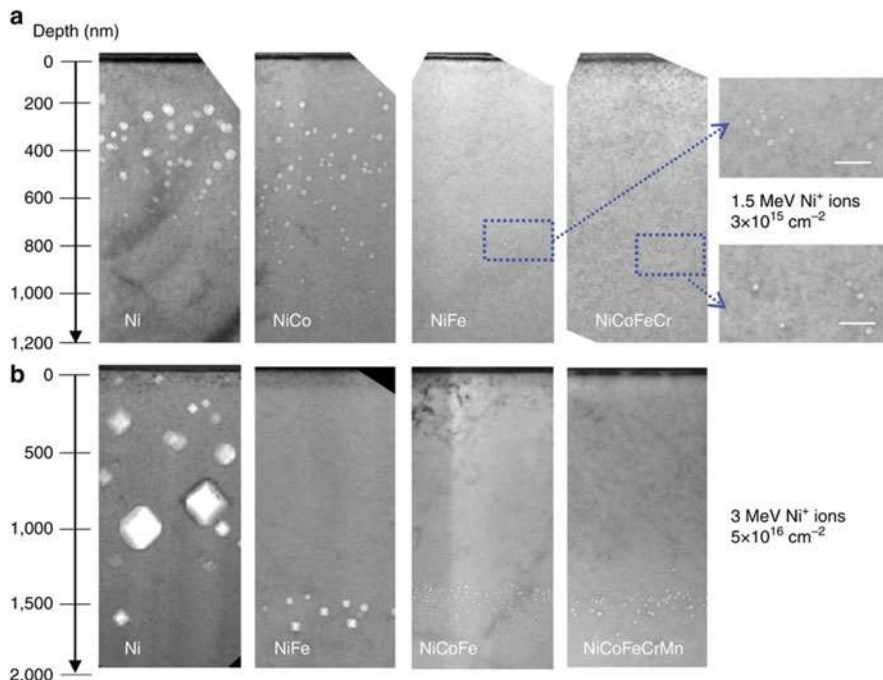


**Fig. 12.15** Void distribution as a function of depth in irradiated pure Ni and Ni-based CSAs. **(a)** Bright-field TEM images of Ni, NiCo, NiFe, and NiCoFeCr after 1.5 MeV  $\text{Ni}^+$  irradiation to  $3 \times 10^{15} \text{ cm}^{-2}$  at 500 °C. **(b)** Bright-field TEM images of Ni, NiFe, NiCoFe, and NiCoFeCrMn after 3 MeV  $\text{Ni}^{2+}$  to  $5 \times 10^{16} \text{ cm}^{-2}$  at 500 °C. (Adapted by Ref. [121])

segregation, but do not change the trend of Ni/Co enrichment and Fe/Cr depletion. Formation and growth of voids requires the incoming flux of vacancies through exchange with Fe/Cr. But the vacancy migration energy through Fe/Cr is much lower than via Ni/Co in NiCoFeCr-based HEAs, so vacancies are less likely to flow to Ni/Co coated voids, and are more likely to diffuse through the Fe/Cr enriched matrix, which suppresses void formation and growth [123]. These factors lead to the void-absent peak damage region. A certain amount of vacancies can migrate to depths beyond the ion-damaged region/dislocation range, where very few interstitial-type defects exist and these migrated vacancies can gradually accumulate to form tiny voids. At very high radiation doses beyond the incubation doses, voids can form in the peak damage region and grow at a steady state, and extended dislocation networks dominate. The evolution of voids and dislocations in Ni-irradiated NiCoFeCr CSA from relatively low to very high doses at 500 °C are shown in Fig. 12.16a–c. Along with the transition from suppressed void formation to obvious void growth in the peak damage region, dislocations develop from isolated loops to extended dislocation networks [109]. This dislocation evolution leads to a closer sink strength of voids and dislocations, unlike the dislocation dominated sink strength at low doses. Overall, the uncommon phenomenon of suppressed void

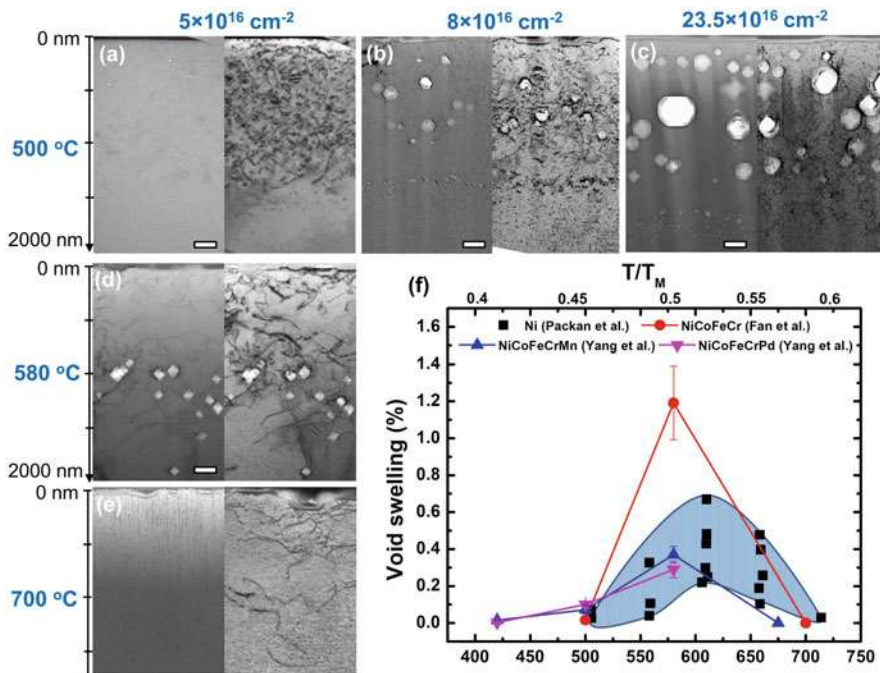


**Fig. 12.16** Microstructure evolution of 3 MeV Ni-ion-irradiated NiCoFeCr CSA under various doses and temperatures. Bright-field TEM images of NiCoFeCr irradiated at 500 °C to (a)  $5 \times 10^{16} \text{ cm}^{-2}$ , (b)  $8 \times 10^{16} \text{ cm}^{-2}$ , and (c)  $23.5 \times 10^{16} \text{ cm}^{-2}$ . Bright-field TEM images of NiCoFeCr irradiated to  $5 \times 10^{16} \text{ cm}^{-2}$  at (d) 580 °C and (e) 700 °C. (f) Void swelling as a function of irradiation temperature for pure Ni [124] and NiCoFeCr-based HEAs [109, 125]. The swelling data of pure Ni was obtained under Ni-ion irradiation to approximate 1 dpa with a dose rate of  $3 \times 10^{-3} \text{ dpa/s}$ . The dose rate for all the NiCoFeCr-based HEAs is  $\sim 3 \times 10^{-3} \text{ dpa/s}$ , but the dose is much higher ( $\sim 54 \text{ dpa}$ ). (Adapted and modified from Ref. [109])

formation in the peak damage region and void formation outside of the ion-damaged region results from the limited mobility of interstitial clusters and preferential diffusion in CSAs/HEAs.

The unusual void distribution at 500 °C is also found in NiCoFeCr CSA irradiated with 3 MeV Ni ions to 54 dpa at 580 °C (Fig. 12.16d). However, voids are absent at 700 °C due to the dissociation of vacancy clusters at such high temperature (Fig. 12.16e). The void swelling evolution in NiCoFeCr CSA, as a function of irradiation temperature, is shown in Fig. 12.16f. As can be observed in the figure, the maximum swelling in NiCoFeCr CSA occurs around 0.5  $T_M$ , which is very similar to the peak swelling temperature of pure Ni. (Please note that  $T_M$  of Ni is slightly higher than NiCoFeCr.) This suggests that knowledge of temperature-dependent void swelling in conventional metals and dilute alloys may be directly used for selection of CSAs/HEAs by considering their  $T_M$ .

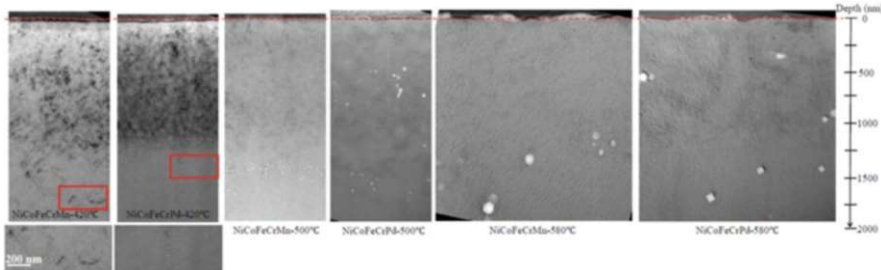


**Fig. 12.17** Bright-field TEM images which show the void distribution in NiCoFeCrPd and NiCoFeCrMn HEAs irradiated with 3 MeV Ni<sup>2+</sup> ions to  $5 \times 10^{16} \text{ cm}^{-2}$  at 420 °C, 500 °C, and 580 °C. (Adapted from Ref. [125])

In addition to the void swelling in NiCoFeCr CSA, Yang et al. [125] also systematically studied the void swelling in NiCoFeCrPd and NiCoFeCrMn HEAs after 3 MeV Ni ion irradiation at temperatures ranging from 420 °C to 580 °C, as shown in Fig. 12.17. They showed suppression in the growth of both voids and dislocation loops in NiCoFeCrPd HEA as compared with NiCoFeCrMn HEA, which is attributed to localized lattice distortion and a higher defect migration barrier in NiCoFeCrPd HEA. Furthermore, the void swelling trend, as a function of temperature in NiCoFeCrPd and NiCoFeCrMn HEAs, is consistent with the trend in NiCoFeCr CSA (Fig. 12.16f). However, it should be noted that the  $T_M$  of NiCoFeCrMn HEA is lower than NiCoFeCr and NiCoFeCrPd. Due to the different  $T_M$ , systematic void swelling studies at various temperatures are required to accurately determine the peak swelling temperature of these alloys and other HEAs. Considering the effects of dose and temperature on the void swelling in NiCoFeCr and other HEAs, one potential strategy to enhance the swelling resistance of CSAs/HEAs may lie in suppressing the void formation in the peak damage region and thus increasing the incubation dose.

It should be mentioned that the aforementioned swelling phenomena were studied under ion irradiation conditions. Thus, the typical limitations of ion irradiation such as the effects of free surface and injected ions exist in these data. As shown in Figs. 12.16 and 12.17, voids are in general absent right below the free surface to a depth of several hundred nanometers. The voids are absent because planar defects such as the free surface, twin boundaries, or grain boundaries reduce the vacancy supersaturation ( $S_v$  in Eq. 12.5) in the vicinity of these defect sinks, creating a void denuded zone (VDZ). For the recombination-dominated void swelling condition, the width of the VDZ ( $d_{VDZ}$ ) is proportional to [126]:

$$d_{VDZ} \sim \left( \frac{D_v}{P} \right)^{0.25} \quad (12.7)$$

where  $P$  is the damage rate, and  $D_v$  is the vacancy diffusivity that is a function of temperature and vacancy migration energy. It has been shown that for NiCoFeCr

CSA irradiated with 3 MeV Ni ions, the measured  $d_{VDZ}$  can be  $\sim 150$  nm at  $500$  °C, and can increase to  $\sim 200$  nm at  $580$  °C [109]. Voids can form at a depth slightly larger than  $d_{VDZ}$ , potentially due to more interstitials lost to the free surface than vacancies at the depth. With a higher temperature, a smaller vacancy migration barrier, and a smaller damage rate,  $d_{VDZ}$  is larger. In the vicinity of the VDZ, both the dislocation and void distribution are affected by the free surface effect and cannot be interpreted solely by the irradiation damage. On the other hand, experimental and theoretical works have shown that the injected ions can suppress void formation and growth in pure metals and steels [127–129]. The injected ions from the ion irradiation can produce extra interstitials that can recombine with vacancies and thus suppress the void swelling at certain depths. Moreover, the effect of injected ions can be affected by temperature, displacement rate, ion energy, and materials properties. The highest concentration of implanted ions, in general, slightly lags the peak displacement damage. These implanted ions can recombine with irradiation-induced vacancies and substantially reduce the void swelling locally, which in turn shifts the peak swelling region to shallower depth. Yang et al. [130] compared the effects of injected ions in pure Ni with NiCo, NiFe, and NiCoFeCr CSAs irradiated with 3 MeV Ni ions at  $500$  °C, and found that the void suppression effect is more significant in pure Ni and NiCo than in NiFe and NiCoFeCr. In their study, the maximum concentration of injected Ni ions can be as high as  $\sim 0.3$  at.% ( $1.5 \times 10^{16} \text{ cm}^{-2}$ ) and 1 at.% ( $5 \times 10^{16} \text{ cm}^{-2}$ ). Such a high concentration of injected ions will create extra interstitials that will recombine with vacancies and inhibit void growth. As shown in Fig. 12.18, a clear VDZ exists in NiCo CSA due to the void suppression effect from injected ions. However, the absence of voids in NiFe and NiCoFeCr CSAs in Fig. 12.18, in the whole ion-damaged region under this dose, is largely due to limited mobility of interstitial clusters and preferential diffusion, as discussed earlier. When the radiation dose further increases, large voids can form and grow in the ion-damaged region in the NiCoFeCr CSA. Under these higher doses, the VDZ due to injected ions can also be observed, although their residing depth changes with dose, as can be seen in Fig. 12.16b, c. Therefore, while ion irradiation allows for the rapid examination of void swelling in alloys such as CSAs/HEAs with well-controlled parameters, the limitations of ion irradiation should be considered when interpreting swelling phenomena in these materials. For 3 MeV Ni ion irradiation at  $500$  °C with a dose rate of  $\sim 10^{-3}$  dpa/s, the useful analysis window may only range from 400 to 600 nm. Increasing the irradiation dose or temperature will further reduce the size of this window. To alleviate the effects of free surface or injected interstitials, it is suggested that energetic ions with higher energy are employed for future ion irradiation studies on CSAs/HEAs.

When the irradiation dose is much lower than the incubation dose, large voids and dislocation networks do not form. Studies have showed suppressed dislocation mobility and growth in CSAs/HEAs under low doses at elevated temperatures. For instance, compared with conventional FeCrNi austenitic steels, dislocation loop density in  $\text{Fe}_{0.27}\text{Ni}_{0.28}\text{Mn}_{0.27}\text{Cr}_{0.18}$  CSA irradiated with 3 or 5.8 MeV Ni ions up to 10 dpa from 400 to  $700$  °C decreases less significantly at higher temperatures due to more sluggish diffusion [71, 87]. Besides, due to the enhanced recombination of

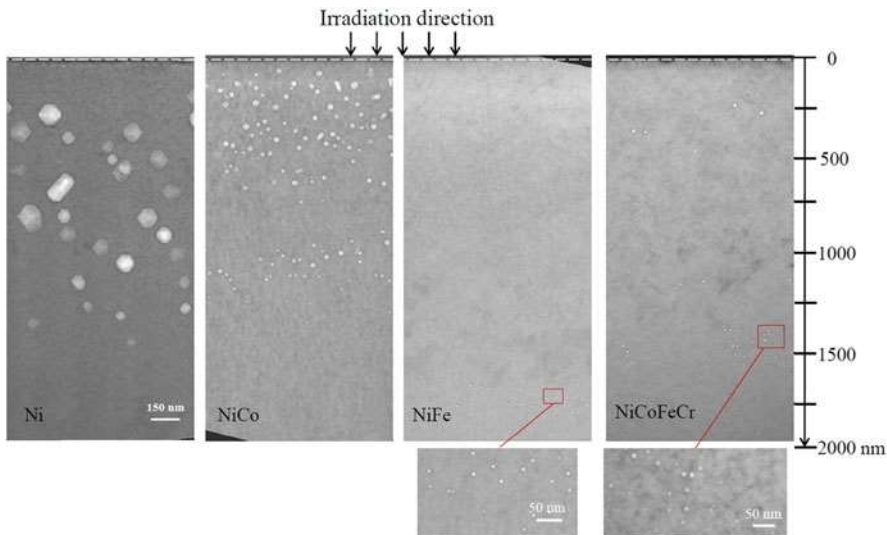


**Fig. 12.18** Bright-field TEM images show the void distribution in pure Ni, NiCo, NiFe, and NiCoFeCr irradiated with 3 MeV  $\text{Ni}^{2+}$  ions to  $1.5 \times 10^{16} \text{ cm}^{-2}$  at  $500^\circ\text{C}$ . (Adapted from Ref. [130])

interstitials and vacancies, the concentration of point defects estimated from the visible dislocation loops in  $\text{Fe}_{0.27}\text{Ni}_{0.28}\text{Mn}_{0.27}\text{Cr}_{0.18}$  CSA is also much lower than conventional FeCrNi steels. Shi et al. [131] studied the glide of dislocation loops in a series of Ni-based CSAs in situ irradiated with 1 MeV Kr ions at  $500^\circ\text{C}$  under TEM. For the observed dislocation loop glide, the jumping distance and frequency of dislocation loops are reduced from Ni to NiCo, to NiFe, and to NiCoFeCr, as shown in Fig. 12.19. This trend suggests that with the increase of chemical complexity, the loop mobility is decreased. The trend of decreased loop mobility in these alloys matches the trend of suppressed void swelling in these alloys, as shown in Fig. 12.15. Moreover, they found no measurable dislocation loop glide in NiCoCr, NiCoFeCrMn, and NiCoFeCrPd under the irradiation condition. Shi et al. [132] also measured the defect density in these alloys irradiated with 1 MeV Kr ions at  $500^\circ\text{C}$  through in situ TEM characterization. Figure 12.20 shows that despite the slight change of slope with increasing dose, the overall defect density decreases from Ni to NiCo, to NiFe, to NiCoFeCr, and to NiCoFeCrPd. The suppressed mobility and growth of dislocation loops due to tuned chemical complexity are manifested in the different types of loops formed, the ratio of perfect to faulted loops, and the loop size (more details can be found in [131, 132]). Recently, under similar in situ TEM irradiation conditions, Parkin et al. [133] demonstrated that the defect density in  $\text{Fe}_{0.27}\text{Ni}_{0.28}\text{Mn}_{0.27}\text{Cr}_{0.18}$  and  $\text{Fe}_{0.35}\text{Ni}_{0.35}\text{Mn}_{0.15}\text{Cr}_{0.15}$  CSAs is comparable to the defect density in NiCoFeCrMn and NiCoFeCrPd HEAs from 0 to 2 dpa. In general, all these studies demonstrated suppressed dislocation mobility and growth in HEAs

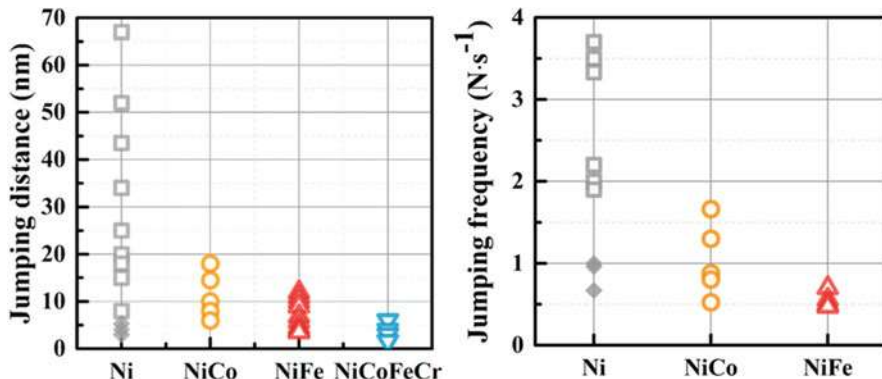
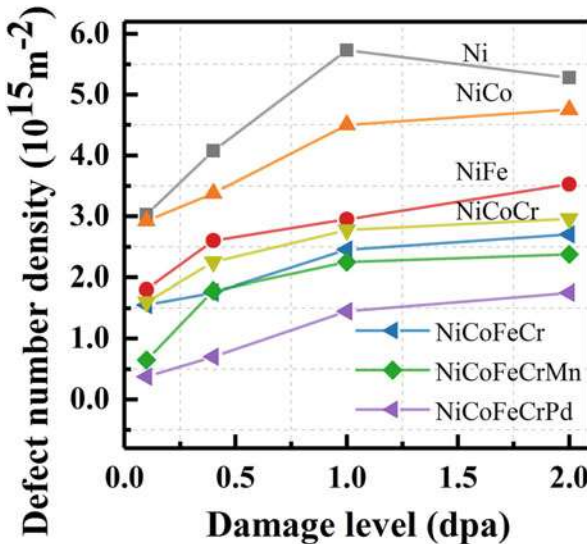


**Fig. 12.19** Jumping distance and frequency of dislocation loop glide in Ni-based CSAs in situ irradiated with 1 MeV Kr ions at 500 °C under TEM. (Adapted from Ref. [131])

**Fig. 12.20** Overall defect density, as a function of dose, in Ni-based CSAs in situ irradiated with 1 MeV Kr ions at 500 °C under TEM. (Adapted from Ref. [132])



and complexed CSAs, as compared with pure metals and less complex CSAs. It will be important to understand if the suppressed dislocation growth in HEAs would be sustained when the incubation dose is exceeded. Furthermore, elucidating how the dislocation growth rate in HEAs compares to that of conventional austenite steels during prolonged irradiation can help guide the design of swelling-resistant HEAs. Current studies suggest that tuning the chemical environments through composition and introducing defect sinks through microstructure engineering are expected to further enhance the overall radiation tolerance of CSAs/HEAs.

## 12.4 Summary and Outlook

This chapter discusses the fundamental defect properties and microstructure evolution in irradiated CSAs/HEAs. The core strength of these materials in terms of their radiation resistance depend strongly on the highly tunable defect properties through chemical composition and concentration. Enhanced defect recombination, limited defect mobility, and preferential diffusion, in general, can lead to more suppressed radiation damage, smaller helium bubbles, and reduced void swelling in complex CSAs/HEAs, as compared with conventional metals and dilute alloys. On the other hand, radiation-induced segregation and substantial void growth in CSAs/HEAs at very high doses, beyond the incubation dose, resemble those phenomena in conventional metals and dilute alloys. Most of the reviewed research studied single-phase CSAs/HEAs that are better positioned to reveal their inherent radiation response. However, in practice, more complex CSAs/HEAs with a sophisticated microstructure may render enhanced properties and therefore deserve future investigations. Our discussion mainly focuses on the irradiation-induced microstructure evolution in face-centered cubic alloys because of the abundant experimental and modeling results. The very high strength and melting temperatures of body-centered cubic CSAs/HEAs could make them attractive for very high temperature nuclear applications. Therefore, more systematic studies on their radiation response are needed [134–137]. Due to the difficulty of studying neutron-irradiated samples, most of the experimental works so far rely on electron or ion irradiation studies. A recent study has showed that after low-dose neutron irradiation, the mechanical property evolution of NiFeMnCr CSA is similar to conventional austenitic stainless steels; however, solute diffusion in the CSA is more sluggish [138]. In-depth understanding of the neutron irradiation response of CSAs/HEAs is needed and could accelerate their applications as nuclear structural materials. Synergistic efforts to evaluate the performance of CSAs/HEAs against corrosion, irradiation-assisted stress corrosion cracking, and creep are also necessary. The wide range of elements and unlimited combinations available to form stable CSAs/HEAs theoretically permit the design of an almost unlimited number of CSAs/HEAs, but how to practically screen robust alloys for nuclear energy applications requires rigorous design principles. The complex chemical environments in CSAs/HEAs call for the-state-of-art instruments for fabrication, characterization, and testing, and demand advanced modeling tools to simulate the defect evolution under radiation. The significant amount of knowledge on the radiation response of conventional nuclear materials paves the foundation for design of CSAs/HEAs for nuclear applications, and new knowledge learned through investigating the radiation resistance of CSAs/HEAs can eventually contribute to safer, economically efficient, and environmentally friendly nuclear energy systems.

## References

1. S.J. Zinkle, G.S. Was, Materials challenges in nuclear energy. *Acta Mater.* **61**(3), 735–758 (2013)
2. S.J. Zinkle, J.T. Busby, Structural materials for fission & fusion energy. *Mater. Today* **12**(11), 12–19 (2009)
3. I.J. Beyerlein, A. Caro, M.J. Demkowicz, N.A. Mara, A. Misra, B.P. Uberuaga, Radiation damage tolerant nanomaterials. *Mater. Today* **16**(11), 443–449 (2013)
4. G. Odette, M. Alinger, B. Wirth, Recent developments in irradiation-resistant steels. *Annu. Rev. Mater. Res.* **38**, 471–503 (2008)
5. G.R. Odette, N.J. Cunningham, T. Stan, M.E. Alam, Y. De Carlan, Chapter 12: Nano-oxide dispersion-strengthened steels, in *Structural Alloys for Nuclear Energy Applications*, ed. by G. R. Odette, S. J. Zinkle, (Elsevier, Boston, 2019), pp. 529–583
6. T. Nagase, P.D. Rack, J.H. Noh, T. Egami, In-situ TEM observation of structural changes in nano-crystalline CoCrCuFeNi multicomponent high-entropy alloy (HEA) under fast electron irradiation by high voltage electron microscopy (HVEM). *Intermetallics* **59**, 32–42 (2015)
7. Y. Zhang, G.M. Stocks, K. Jin, C. Lu, H. Bei, B.C. Sales, L. Wang, L.K. Béland, R.E. Stoller, G.D. Samolyuk, M. Caro, A. Caro, W.J. Weber, Influence of chemical disorder on energy dissipation and defect evolution in concentrated solid solution alloys. *Nat. Commun.* **6**, 8736 (2015)
8. C. Lu, L. Niu, N. Chen, K. Jin, T. Yang, P. Xiu, Y. Zhang, F. Gao, H. Bei, S. Shi, M.-R. He, I.M. Robertson, W.J. Weber, L. Wang, Enhancing radiation tolerance by controlling defect mobility and migration pathways in multicomponent single-phase alloys. *Nat. Commun.* **7**, 13564 (2016)
9. K. Jin, C. Lu, L.M. Wang, J. Qu, W.J. Weber, Y. Zhang, H. Bei, Effects of compositional complexity on the ion-irradiation induced swelling and hardening in Ni-containing equiatomic alloys. *Scripta Mater.* **119**, 65–70 (2016)
10. Y. Zhang, *High-Entropy Materials* (Springer, 2019)
11. O.N. Senkov, J.D. Miller, D.B. Miracle, C. Woodward, Accelerated exploration of multi-principal element alloys with solid solution phases. *Nat. Commun.* **6**, 7529 (2015)
12. B.S. Murty, J.-W. Yeh, S. Ranganathan, P. Bhattacharjee, *High-Entropy Alloys* (Elsevier, 2019)
13. M.C. Gao, J.-W. Yeh, P.K. Liaw, Y. Zhang, *High-Entropy Alloys* (Springer, Cham, 2016)
14. S. Mu, Z. Pei, X. Liu, G.M. Stocks, Electronic transport and phonon properties of maximally disordered alloys: From binaries to high-entropy alloys. *J. Mater. Res.* **33**(19), 2857–2880 (2018)
15. Y. Tong, S. Zhao, K. Jin, H. Bei, J.Y.P. Ko, Y. Zhang, F.X. Zhang, A comparison study of local lattice distortion in Ni80Pd20 binary alloy and FeCoNiCrPd high-entropy alloy. *Scripta Mater.* **156**, 14–18 (2018)
16. Y. Zhang, T. Egami, W.J. Weber, Dissipation of radiation energy in concentrated solid-solution alloys: Unique defect properties and microstructural evolution. *MRS Bull.* **44**(10), 798–811 (2019)
17. T. Egami, M. Ojha, O. Khorgolkhuu, D. Nicholson, G. Stocks, Local electronic effects and irradiation resistance in high-entropy alloys. *JOM* **67**(10), 2345–2349 (2015)
18. Y. Tong, S. Zhao, H. Bei, T. Egami, Y. Zhang, F. Zhang, Severe local lattice distortion in Zr- and/or Hf-containing refractory multi-principal element alloys. *Acta Mater.* **183**, 172–181 (2020)
19. W. Chen, X. Ding, Y. Feng, X. Liu, K. Liu, Z.P. Lu, D. Li, Y. Li, C.T. Liu, X.-Q. Chen, Vacancy formation enthalpies of high-entropy FeCoCrNi alloy via first-principles calculations and possible implications to its superior radiation tolerance. *J. Mater. Sci. Technol.* **34**(2), 355–364 (2018)

20. J.W. Yeh, S.K. Chen, S.J. Lin, J.Y. Gan, T.S. Chin, T.T. Shun, C.H. Tsau, S.Y. Chang, Nanostructured high-entropy alloys with multiple principal elements: Novel alloy design concepts and outcomes. *Adv. Eng. Mater.* **6**(5), 299–303 (2004)
21. G.S. Was, *Fundamentals of Radiation Materials Science: Metals and Alloys* (Springer, 2016)
22. K. Nordlund, S.J. Zinkle, A.E. Sand, F. Granberg, R.S. Averback, R.E. Stoller, T. Suzudo, L. Malerba, F. Banhart, W.J. Weber, F. Willaime, S.L. Dudarev, D. Simeone, Primary radiation damage: A review of current understanding and models. *J. Nucl. Mater.* **512**, 450–479 (2018)
23. W. Wolfer, Fundamental properties of defects in metals. *Compr. Nucl. Mater.* **1**, 1–45 (2012)
24. Y. Chimi, A. Iwase, N. Ishikawa, N. Kuroda, T. Kambara, Radiation annealing induced by electronic excitation in iron. *Nucl. Instrum. Methods Phys. Res. B* **164–165**, 408–414 (2000)
25. Z.G. Wang, C. Dufour, E. Paumier, M. Toulemonde, Defects in metals induced by nuclear collisions and their modifications by swift heavy ion irradiations. *Nucl. Instrum. Methods Phys. Res. B* **115**(1), 577–580 (1996)
26. K. Nordlund, R.S. Averback, Collision cascades in metals and semiconductors: Defect creation and interface behavior. *J. Nucl. Mater.* **276**(1), 194–201 (2000)
27. T.D. de la Rubia, M.W. Guinan, Progress in the development of a molecular dynamics code for high-energy cascade studies. *J. Nucl. Mater.* **174**(2), 151–157 (1990)
28. A. Duvenbeck, A. Wucher, Low-energy electronic excitation in atomic collision cascades: A nonlinear transport model. *Phys. Rev. B* **72**(16), 165408 (2005)
29. A.M. Rutherford, D.M. Duffy, The effect of electron-ion interactions on radiation damage simulations. *J. Phys. Condens. Matter* **19**(49), 496201 (2007)
30. Y. Zhang, W.J. Weber, Ion irradiation and modification: The role of coupled electronic and nuclear energy dissipation and subsequent nonequilibrium processes in materials. *Appl. Phys. Rev.* **7**(4), 041307 (2020)
31. N. Sellami, A. Debelle, M.W. Ullah, H.M. Christen, J.K. Keum, H. Bei, H. Xue, W.J. Weber, Y. Zhang, Effect of electronic energy dissipation on strain relaxation in irradiated concentrated solid solution alloys. *Curr. Opin. Solid State Mater. Sci.* **23**(2), 107–115 (2019)
32. E. Zarkadoula, G. Samolyuk, W.J. Weber, Effects of electronic excitation on cascade dynamics in nickel–iron and nickel–palladium systems. *Scripta Mater.* **138**, 124–129 (2017)
33. E. Zarkadoula, G. Samolyuk, H. Xue, H. Bei, W.J. Weber, Effects of two-temperature model on cascade evolution in Ni and NiFe. *Scripta Mater.* **124**, 6–10 (2016)
34. E. Zarkadoula, G. Samolyuk, W.J. Weber, Effects of electronic excitation in 150 keV Ni ion irradiation of metallic systems. *AIP Adv.* **8**(1), 015121 (2018)
35. K. Jin, S. Mu, K. An, W.D. Porter, G.D. Samolyuk, G.M. Stocks, H. Bei, Thermophysical properties of Ni-containing single-phase concentrated solid solution alloys. *Mater. Des.* **117**, 185–192 (2017)
36. S. Mu, G.D. Samolyuk, S. Wimmer, M.C. Troparevsky, S.N. Khan, S. Mankovsky, H. Ebert, G.M. Stocks, Uncovering electron scattering mechanisms in NiFeCoCrMn derived concentrated solid solution and high entropy alloys. *npj Comput. Mater.* **5**(1), 1 (2019)
37. H.C. Robarts, T.E. Millichamp, D.A. Lagos, J. Laverock, D. Billington, J.A. Duffy, D. O'Neill, S.R. Giblin, J.W. Taylor, G. Kontrym-Sznajd, M. Samsel-Czekala, H. Bei, S. Mu, G.D. Samolyuk, G.M. Stocks, S.B. Dugdale, Extreme Fermi surface smearing in a maximally disordered concentrated solid solution. *Phys. Rev. Lett.* **124**(4), 046402 (2020)
38. Y. Tong, G. Velisa, S. Zhao, W. Guo, T. Yang, K. Jin, C. Lu, H. Bei, J.Y.P. Ko, D.C. Pagan, Y. Zhang, L. Wang, F.X. Zhang, Evolution of local lattice distortion under irradiation in medium- and high-entropy alloys. *Materialia* **2**, 73–81 (2018)
39. E. Zarkadoula, G. Samolyuk, W.J. Weber, Effects of electron-phonon coupling and electronic thermal conductivity in high energy molecular dynamics simulations of irradiation cascades in nickel. *Comput. Mater. Sci.* **162**, 156–161 (2019)
40. B.L. Gyorffy, Coherent-potential approximation for a nonoverlapping-muffin-tin-potential model of random substitutional alloys. *Phys. Rev. B* **5**(6), 2382–2384 (1972)

41. J.M. Sanchez, F. Ducastelle, D. Gratias, Generalized cluster description of multicomponent systems. *Phys. A Stat. Mech. Appl.* **128**(1), 334–350 (1984)
42. A. Zunger, S.H. Wei, L.G. Ferreira, J.E. Bernard, Special quasirandom structures. *Phys. Rev. Lett.* **65**(3), 353–356 (1990)
43. S. Mu, S. Wimmer, S. Mankovsky, H. Ebert, G.M. Stocks, Influence of local lattice distortions on electrical transport of refractory high entropy alloys. *Scr. Mater.* **170**, 189–194 (2019)
44. S. Zhao, W.J. Weber, Y. Zhang, Unique challenges for modeling defect dynamics in concentrated solid-solution alloys. *JOM* **69**(11), 2084–2091 (2017)
45. J. Ding, Q. Yu, M. Asta, R.O. Ritchie, Tunable stacking fault energies by tailoring local chemical order in CrCoNi medium-entropy alloys. *PNAS* **115**(36), 8919–8924 (2018)
46. X. Zhang, M.H.F. Sluiter, Ab initio prediction of vacancy properties in concentrated alloys: The case of fcc Cu-Ni. *Phys. Rev. B* **91**(17), 174107 (2015)
47. A. Van der Ven, G. Ceder, Vacancies in ordered and disordered binary alloys treated with the cluster expansion. *Phys. Rev. B* **71**(5), 054102 (2005)
48. S.C. Middleburgh, D.M. King, G.R. Lumpkin, M. Cortie, L. Edwards, Segregation and migration of species in the CrCoFeNi high entropy alloy. *J. Alloys Compd.* **599**, 179–182 (2014)
49. J.B. Piochaud, T.P.C. Klaver, G. Adjanor, P. Olsson, C. Domain, C.S. Becquart, First-principles study of point defects in an fcc Fe-10Ni-20Cr model alloy. *Phys. Rev. B* **89**(2), 024101 (2014)
50. S. Zhao, G.M. Stocks, Y. Zhang, Defect energetics of concentrated solid-solution alloys from ab initio calculations: Ni0.5Co0.5, Ni0.5Fe0.5, Ni0.8Fe0.2 and Ni0.8Cr0.2. *Phys. Chem. Chem. Phys.* **18**(34), 24043–24056 (2016)
51. S. Zhao, T. Egami, G.M. Stocks, Y. Zhang, Effect of d electrons on defect properties in equiatomic NiCoCr and NiCoFeCr concentrated solid solution alloys. *Phys. Rev. Mater.* **2**(1), 013602 (2018)
52. G. Henkelman, B.P. Uberuaga, H. Jónsson, A climbing image nudged elastic band method for finding saddle points and minimum energy paths. *J. Chem. Phys.* **113**(22), 9901–9904 (2000)
53. S. Zhao, Y. Osetsky, Y. Zhang, Preferential diffusion in concentrated solid solution alloys: NiFe, NiCo and NiCoCr. *Acta Mater.* **128**, 391–399 (2017)
54. P. Pulay, Convergence acceleration of iterative sequences. The case of scf iteration. *Chem. Phys. Lett.* **73**(2), 393–398 (1980)
55. S. Zhao, Y. Osetsky, A.V. Barashev, Y. Zhang, Frenkel defect recombination in Ni and Ni-containing concentrated solid-solution alloys. *Acta Mater.* **173**, 184–194 (2019)
56. Y.N. Osetsky, L.K. Béland, R.E. Stoller, Specific features of defect and mass transport in concentrated fcc alloys. *Acta Mater.* **115**, 364–371 (2016)
57. C. Lu, T. Yang, L. Niu, Q. Peng, K. Jin, M.L. Crespillo, G. Velisa, H. Xue, F. Zhang, P. Xiu, Interstitial migration behavior and defect evolution in ion irradiated pure nickel and Ni-xFe binary alloys. *J. Nucl. Mater.* **509**, 237–244 (2018)
58. K. Nordlund, J. Wallenius, L. Malerba, Molecular dynamics simulations of threshold displacement energies in Fe. *Nucl. Instrum. Methods Phys. Res. B* **246**(2), 322–332 (2006)
59. J. Fu, W. Ding, M. Zheng, X. Mao, Molecular dynamics study on threshold displacement energies in Fe-Cr alloys. *Nucl. Instrum. Methods Phys. Res. B* **419**, 1–7 (2018)
60. N. Juslin, K. Nordlund, J. Wallenius, L. Malerba, Simulation of threshold displacement energies in FeCr. *Nucl. Instrum. Methods Phys. Res. B* **255**(1), 75–77 (2007)
61. D.J. Bacon, Y.N. Osetsky, R. Stoller, R.E. Voskoboinikov, MD description of damage production in displacement cascades in copper and  $\alpha$ -iron. *J. Nucl. Mater.* **323**(2), 152–162 (2003)
62. S. Zhao, B. Liu, G.D. Samolyuk, Y. Zhang, W.J. Weber, Alloying effects on low-energy recoil events in concentrated solid-solution alloys. *J. Nucl. Mater.* **529**, 151941 (2020)
63. D.M. Duffy, A.M. Rutherford, Including the effects of electronic stopping and electron-ion interactions in radiation damage simulations. *J. Phys. Condens. Matt.* **19**(1), 016207 (2006)

64. E. Zarkadoula, G. Samolyuk, W.J. Weber, Two-temperature model in molecular dynamics simulations of cascades in Ni-based alloys. *J. Alloys Compd.* **700**, 106–112 (2017)
65. E. Zarkadoula, S.L. Daraszewicz, D.M. Duffy, M.A. Seaton, I.T. Todorov, K. Nordlund, M.T. Dove, K. Trachenko, Electronic effects in high-energy radiation damage in iron. *J. Phys. Condens. Matt.* **26**(8), 085401 (2014)
66. G. Veliş, M.W. Ullah, H. Xue, K. Jin, M.L. Crespillo, H. Bei, W.J. Weber, Y. Zhang, Irradiation-induced damage evolution in concentrated Ni-based alloys. *Acta Mater.* **135**, 54–60 (2017)
67. K. Nordlund, R.S. Averback, Inverse Kirkendall mixing in collision cascades. *Phys. Rev. B* **59**(1), 20–23 (1999)
68. G. Bonny, D. Chakraborty, S. Pandey, A. Manzoor, N. Castin, S.R. Phillpot, D.S. Aidhy, Classical interatomic potential for quaternary Ni–Fe–Cr–Pd solid solution alloys. *Model. Simul. Mater. Sci. Eng.* **26**(6), 065014 (2018)
69. Y. Lin, T. Yang, L. Lang, C. Shan, H. Deng, W. Hu, F. Gao, Enhanced radiation tolerance of the Ni–Co–Cr–Fe high-entropy alloy as revealed from primary damage. *Acta Mater.* **196**, 133–143 (2020)
70. T.-n. Yang, C. Lu, G. Velisa, K. Jin, P. Xiu, M.L. Crespillo, Y. Zhang, H. Bei, L. Wang, Effect of alloying elements on defect evolution in Ni–20X binary alloys. *Acta Mater.* **151**, 159–168 (2018)
71. T. Yang, C. Li, S.J. Zinkle, S. Zhao, H. Bei, Y. Zhang, Irradiation responses and defect behavior of single-phase concentrated solid solution alloys. *J. Mater. Res.* **33**(19), 3077–3091 (2018)
72. Y. Tong, F. Zhang, Critical review of chemical complexity effect on local structure of multi-principal-element alloys. *JOM* **71**(10), 3419–3423 (2019)
73. S. Zhao, Y. Osetsky, Y. Zhang, Diffusion of point defects in ordered and disordered Ni–Fe alloys. *J. Alloys Compd.* **805**, 1175–1183 (2019)
74. S. Zinkle, 1.03-radiation-induced effects on microstructure. *Compr. Nucl. Mater.* **1**, 65–98 (2012)
75. S.J. Zinkle, Y. Matsukawa, Observation and analysis of defect cluster production and interactions with dislocations. *J. Nucl. Mater.* **329**, 88–96 (2004)
76. L.K. Mansur, Void swelling in metals and alloys under irradiation: An assessment of the theory. *Nucl. Technol.* **40**(1), 5–34 (1978)
77. F. Garner, Evolution of microstructure in face-centered cubic metals during irradiation. *J. Nucl. Mater.* **205**, 98–117 (1993)
78. H. Matsui, Microstructural evolution in BCC metals and alloys under irradiation. *Radiat. Eff. Defects Solids* **148**(1–4), 515–516 (1999)
79. B. Singh, S. Zinkle, Defect accumulation in pure fcc metals in the transient regime: A review. *J. Nucl. Mater.* **206**(2–3), 212–229 (1993)
80. S. Zinkle, P. Maziasz, R. Stoller, Dose dependence of the microstructural evolution in neutron-irradiated austenitic stainless steel. *J. Nucl. Mater.* **206**(2–3), 266–286 (1993)
81. L. Tan, R.E. Stoller, K.G. Field, Y. Yang, H. Nam, D. Morgan, B. Wirth, M. Gussev, J. Busby, Microstructural evolution of type 304 and 316 stainless steels under neutron irradiation at LWR relevant conditions. *JOM* **68**(2), 517–529 (2016)
82. P. Maziasz, Overview of microstructural evolution in neutron-irradiated austenitic stainless steels. *J. Nucl. Mater.* **205**, 118–145 (1993)
83. F.A. Garner, Recent insights on the swelling and creep of irradiated austenitic alloys. *J. Nucl. Mater.* **122**(1), 459–471 (1984)
84. X. Zhang, K. Hattar, Y. Chen, L. Shao, J. Li, C. Sun, K. Yu, N. Li, M.L. Taheri, H. Wang, J. Wang, M. Nastasi, Radiation damage in nanostructured materials. *Prog. Mater. Sci.* **96**, 217–321 (2018)
85. O. El-Atwani, N. Li, M. Li, A. Devaraj, J.K.S. Baldwin, M.M. Schneider, D. Sobieraj, J.S. Wróbel, D. Nguyen-Manh, S.A. Maloy, E. Martinez, Outstanding radiation resistance of tungsten-based high-entropy alloys. *Sci. Adv.* **5**(3), eaav2002 (2019)

86. M. Moschetti, A. Xu, B. Schuh, A. Hohenwarter, J.-P. Couzinié, J.J. Kružic, D. Bhattacharyya, B. Gludovatz, On the room-temperature mechanical properties of an ion-irradiated TiZrNbHfTa refractory high entropy alloy. *JOM* **72**(1), 130–138 (2020)
87. N.K. Kumar, C. Li, K. Leonard, H. Bei, S. Zinkle, Microstructural stability and mechanical behavior of FeNiMnCr high entropy alloy under ion irradiation. *Acta Mater.* **113**, 230–244 (2016)
88. G.S. Jawaharam, C.M. Barr, A.M. Monterrosa, K. Hattar, R.S. Averback, S.J. Dillon, Irradiation induced creep in nanocrystalline high entropy alloys. *Acta Mater.* **182**, 68–76 (2020)
89. Y. Zhang, S. Zhao, W.J. Weber, K. Nordlund, F. Granberg, F. Djurabekova, Atomic-level heterogeneity and defect dynamics in concentrated solid-solution alloys. *Curr. Opin. Solid State Mater. Sci.* **21**(5), 221–237 (2017)
90. Y. Zhang, K. Jin, H. Xue, C. Lu, R.J. Olsen, L.K. Béland, M.W. Ullah, S. Zhao, H. Bei, D.S. Aidhy, Influence of chemical disorder on energy dissipation and defect evolution in advanced alloys. *J. Mater. Res.* **31**(16), 2363–2375 (2016)
91. K. Jin, W. Guo, C. Lu, M.W. Ullah, Y. Zhang, W.J. Weber, L. Wang, J.D. Poplawsky, H. Bei, Effects of Fe concentration on the ion-irradiation induced defect evolution and hardening in Ni-Fe solid solution alloys. *Acta Mater.* **121**, 365–373 (2016)
92. K. Jin, H. Bei, Y. Zhang, Ion irradiation induced defect evolution in Ni and Ni-based FCC equiatomic binary alloys. *J. Nucl. Mater.* **471**, 193–199 (2016)
93. C. Lu, K. Jin, L.K. Béland, F. Zhang, T. Yang, L. Qiao, Y. Zhang, H. Bei, H.M. Christen, R.E. Stoller, Direct observation of defect range and evolution in ion-irradiated single crystalline Ni and Ni binary alloys. *Sci. Rep.* **6**, 19994 (2016)
94. Z. Fan, G. Velisa, K. Jin, M.L. Crespillo, H. Bei, W.J. Weber, Y. Zhang, Temperature-dependent defect accumulation and evolution in Ni-irradiated NiFe concentrated solid-solution alloy. *J. Nucl. Mater.* **519**, 1–9 (2019)
95. G. Veliša, E. Wendler, S. Zhao, K. Jin, H. Bei, W. Weber, Y. Zhang, Delayed damage accumulation by athermal suppression of defect production in concentrated solid solution alloys. *Mater. Res. Lett.* **6**(2), 136–141 (2018)
96. F. Zhang, M.W. Ullah, S. Zhao, K. Jin, Y. Tong, G. Velisa, H. Xue, H. Bei, R. Huang, C. Park, Local structure of NiPd solid solution alloys and its response to ion irradiation. *J. Alloys Compd.* **755**(C) (2018)
97. F. Zhang, S. Zhao, K. Jin, H. Xue, G. Velisa, H. Bei, R. Huang, J. Ko, D. Pagan, J. Neufeld, Local structure and short-range order in a NiCoCr solid solution alloy. *Phys. Rev. Lett.* **118**(20), 205501 (2017)
98. Q.-J. Li, H. Sheng, E. Ma, Strengthening in multi-principal element alloys with local-chemical-order roughened dislocation pathways. *Nat. Commun.* **10**(1), 3563 (2019)
99. S. Yin, J. Ding, M. Asta, R.O. Ritchie, Ab initio modeling of the energy landscape for screw dislocations in body-centered cubic high-entropy alloys. *npj Comput. Mater.* **6**(1), 110 (2020)
100. F. Zhang, Y. Tong, G. Velisa, H. Bei, W. Weber, Y. Zhang, Local structure of Ni80X20 (X: Cr, Mn, Pd) solid-solution alloys and its response to ion irradiation. *J. Phys. Condens. Matter* **32**(7), 074002 (2019)
101. Y. Ossetsky, A.V. Barashev, L.K. Béland, Z. Yao, K. Ferasat, Y. Zhang, Tunable chemical complexity to control atomic diffusion in alloys. *npj Comput. Mater.* **6**(1), 1–8 (2020)
102. X. Wang, K. Jin, D. Chen, H. Bei, Y. Wang, W.J. Weber, Y. Zhang, K.L. More, Effects of Fe concentration on helium bubble formation in NiFe<sub>x</sub> single-phase concentrated solid solution alloys. *Materialia* **5**, 100183 (2019)
103. T.R. Allen, J.T. Busby, G.S. Was, E.A. Kenik, On the mechanism of radiation-induced segregation in austenitic Fe–Cr–Ni alloys. *J. Nucl. Mater.* **255**(1), 44–58 (1998)
104. T. Yang, S. Xia, W. Guo, R. Hu, J.D. Poplawsky, G. Sha, Y. Fang, Z. Yan, C. Wang, C. Li, Effects of temperature on the irradiation responses of Al 0.1 CoCrFeNi high entropy alloy. *Scr. Mater.* **144**, 31–35 (2018)

105. C. Lu, T. Yang, K. Jin, N. Gao, P. Xiu, Y. Zhang, F. Gao, H. Bei, W.J. Weber, K. Sun, Radiation-induced segregation on defect clusters in single-phase concentrated solid-solution alloys. *Acta Mater.* **127**, 98–107 (2017)
106. M.-R. He, S. Wang, S. Shi, K. Jin, H. Bei, K. Yasuda, S. Matsumura, K. Higashida, I.M. Robertson, Mechanisms of radiation-induced segregation in CrFeCoNi-based single-phase concentrated solid solution alloys. *Acta Mater.* **126**, 182–193 (2017)
107. C.M. Barr, J.E. Nathaniel, K.A. Unocic, J. Liu, Y. Zhang, Y. Wang, M.L. Taheri, Exploring radiation induced segregation mechanisms at grain boundaries in equiatomic CoCrFeNiMn high entropy alloy under heavy ion irradiation. *Scr. Mater.* **156**, 80–84 (2018)
108. T. Yang, W. Guo, J.D. Poplawsky, D. Li, L. Wang, Y. Li, W. Hu, M.L. Crespi, Z. Yan, Y. Zhang, Y. Wang, S.J. Zinkle, Structural damage and phase stability of Al0.3CoCrFeNi high entropy alloy under high temperature ion irradiation. *Acta Mater.* **188**, 1–15 (2020)
109. Z. Fan, T.-n. Yang, B. Kombaiah, X. Wang, P.D. Edmondson, Y.N. Ossetsky, K. Jin, C. Lu, H. Bei, L. Wang, K.L. More, W.J. Weber, Y. Zhang, From suppressed void growth to significant void swelling in NiCoFeCr complex concentrated solid-solution alloy. *Materialia* **9**, 100603 (2020)
110. G.S. Was, J.P. Wharry, B. Frisbie, B.D. Wirth, D. Morgan, J.D. Tucker, T.R. Allen, Assessment of radiation-induced segregation mechanisms in austenitic and ferritic-martensitic alloys. *J. Nucl. Mater.* **411**(1–3), 41–50 (2011)
111. S. Watanabe, N. Sakaguchi, N. Hashimoto, M. Nakamura, H. Takahashi, C. Namba, N.Q. Lam, Radiation-induced segregation accompanied by grain boundary migration in austenitic stainless steel. *J. Nucl. Mater.* **232**(2), 113–118 (1996)
112. Z. Fan, W. Zhong, K. Jin, H. Bei, Y.N. Ossetsky, Y. Zhang, Diffusion-mediated chemical concentration variation and void evolution in ion-irradiated NiCoFeCr high-entropy alloy. *J. Mater. Res.*, 1–13 (2020)
113. B. Kombaiah, K. Jin, H. Bei, P.D. Edmondson, Y. Zhang, Phase stability of single phase Al0.12CrNiFeCo high entropy alloy upon irradiation. *Mater. Des.* **160**, 1208–1216 (2018)
114. L.J. Santodonato, Y. Zhang, M. Feygenson, C.M. Parish, M.C. Gao, R.J.K. Weber, J.C. Neufeind, Z. Tang, P.K. Liaw, Deviation from high-entropy configurations in the atomic distributions of a multi-principal-element alloy. *Nat. Commun.* **6**(1), 5964 (2015)
115. P.P. Cao, H. Wang, J.Y. He, C. Xu, S.H. Jiang, J.L. Du, X.Z. Cao, E.G. Fu, Z.P. Lu, Effects of nanosized precipitates on irradiation behavior of CoCrFeNi high entropy alloys. *J. Alloys Compd.* **859**, 158291 (2021)
116. Z. Fan, S. Zhao, K. Jin, D. Chen, Y.N. Ossetskiy, Y. Wang, H. Bei, K.L. More, Y. Zhang, Helium irradiated cavity formation and defect energetics in Ni-based binary single-phase concentrated solid solution alloys. *Acta Mater.* **164**, 283–292 (2019)
117. D. Chen, Y. Tong, H. Li, J. Wang, Y. Zhao, A. Hu, J. Kai, Helium accumulation and bubble formation in FeCoNiCr alloy under high fluence He<sup>+</sup> implantation. *J. Nucl. Mater.* **501**, 208–216 (2018)
118. D. Chen, S. Zhao, J. Sun, P. Tai, Y. Sheng, Y. Zhao, G. Yeli, W. Lin, S. Liu, W. Kai, Diffusion-controlled helium bubble formation resistance of FeCoNiCr high-entropy alloy in the half-melting temperature regime. *J. Nucl. Mater.* **526**, 151747 (2019)
119. L. Yang, H. Ge, J. Zhang, T. Xiong, Q. Jin, Y. Zhou, X. Shao, B. Zhang, Z. Zhu, S. Zheng, X. Ma, High He-ion irradiation resistance of CrMnFeCoNi high-entropy alloy revealed by comparison study with Ni and 304SS. *J. Mater. Sci. Technol.* **35**(3), 300–305 (2019)
120. S. Zhao, D. Chen, J.-J. Kai, First-principles study of He behavior in a NiCoFeCr concentrated solid-solution alloy. *Mater. Res. Lett.* **7**(5), 188–193 (2019)
121. C. Lu, L. Niu, N. Chen, K. Jin, T. Yang, P. Xiu, Y. Zhang, F. Gao, H. Bei, S. Shi, Enhancing radiation tolerance by controlling defect mobility and migration pathways in multicomponent single-phase alloys. *Nat. Commun.* **7**, 13564 (2016)
122. S. Zhao, G.M. Stocks, Y. Zhang, Defect energetics of concentrated solid-solution alloys from ab initio calculations: Ni 0.5 Co 0.5, Ni 0.5 Fe 0.5, Ni 0.8 Fe 0.2 and Ni 0.8 Cr 0.2. *PCCP* **18**(34), 24043–24056 (2016)

123. A. Barashev, Y. Ossetsky, H. Bei, C. Lu, L. Wang, Y. Zhang, Chemically-biased diffusion and segregation impede void growth in irradiated Ni-Fe alloys. *Curr. Opin. Solid State Mater. Sci.* **23**(2), 92–100 (2019)
124. N. Packan, K. Farrell, J. Stiegler, Correlation of neutron and heavy-ion damage: I. The influence of dose rate and injected helium on swelling in pure nickel. *J. Nucl. Mater.* **78**(1), 143–155 (1978)
125. T.-N. Yang, C. Lu, G. Velisa, K. Jin, P. Xiu, Y. Zhang, H. Bei, L. Wang, Influence of irradiation temperature on void swelling in NiCoFeCrMn and NiCoFeCrPd. *Scr. Mater.* **158**, 57–61 (2019)
126. S. Zinkle, L. Snead, Opportunities and limitations for ion beams in radiation effects studies: Bridging critical gaps between charged particle and neutron irradiations. *Scr. Mater.* **143**, 154–160 (2018)
127. L. Shao, C.-C. Wei, J. Gigax, A. Aitkaliyeva, D. Chen, B. Sencer, F. Garner, Effect of defect imbalance on void swelling distributions produced in pure iron irradiated with 3.5 MeV self-ions. *J. Nucl. Mater.* **453**(1–3), 176–181 (2014)
128. C. Sun, F.A. Garner, L. Shao, X. Zhang, S. Maloy, Influence of injected interstitials on the void swelling in two structural variants of 304L stainless steel induced by self-ion irradiation at 500 C. *Nucl. Instrum. Methods Phys. Res., Sect. B* **409**, 323–327 (2017)
129. P.J. Doyle, K.M. Benensky, S.J. Zinkle, Modeling the impact of radiation-enhanced diffusion on implanted ion profiles. *J. Nucl. Mater.* **509**, 168–180 (2018)
130. T.-N. Yang, C. Lu, K. Jin, M.L. Crespillo, Y. Zhang, H. Bei, L. Wang, The effect of injected interstitials on void formation in self-ion irradiated nickel containing concentrated solid solution alloys. *J. Nucl. Mater.* **488**, 328–337 (2017)
131. S. Shi, H. Bei, I.M. Robertson, Impact of alloy composition on one-dimensional glide of small dislocation loops in concentrated solid solution alloys. *Mater. Sci. Eng. A* **700**, 617–621 (2017)
132. S. Shi, M.-R. He, K. Jin, H. Bei, I.M. Robertson, Evolution of ion damage at 773K in Ni-containing concentrated solid-solution alloys. *J. Nucl. Mater.* **501**, 132–142 (2018)
133. C. Parkin, M. Moorehead, M. Elbakhshwan, K. Sridharan, A. Couet, J. Hu, W.-Y. Chen, M. Li, L. He, In situ microstructural evolution in face-centered and body-centered cubic complex concentrated solid-solution alloys under heavy ion irradiation. *Acta. Mater.* **198**, 85–99 (2020)
134. O. Senkov, G. Wilks, D. Miracle, C. Chuang, P. Liaw, Refractory high-entropy alloys. *Intermetallics* **18**(9), 1758–1765 (2010)
135. Y. Lu, H. Huang, X. Gao, C. Ren, J. Gao, H. Zhang, S. Zheng, Q. Jin, Y. Zhao, C. Lu, T. Wang, T. Li, A promising new class of irradiation tolerant materials: Ti<sub>2</sub>ZrHfV<sub>0.5</sub>Mo<sub>0.2</sub> high-entropy alloy. *J. Mater. Sci. Technol.* **35**(3), 369–373 (2019)
136. D. Patel, M.D. Richardson, B. Jim, S. Akhmadaliev, R. Goodall, A.S. Gandy, Radiation damage tolerance of a novel metastable refractory high entropy alloy V2.5Cr1.2WMoCo0.04. *J. Nucl. Mater.* **531**, 152005 (2020)
137. Y. Zhang, T.T. Zuo, Z. Tang, M.C. Gao, K.A. Dahmen, P.K. Liaw, Z.P. Lu, Microstructures and properties of high-entropy alloys. *Prog. Mater. Sci.* **61**, 1–93 (2014)
138. C. Li, X. Hu, T. Yang, N.A.P.K. Kumar, B.D. Wirth, S.J. Zinkle, Neutron irradiation response of a Co-free high entropy alloy. *J. Nucl. Mater.* **527**, 151838 (2019)